A FORCE AND DISPLACEMENT SELF-SENSING METHOD FOR A MRI COMPATIBLE TWEEZER END EFFECTOR

A Thesis
Presented to
The Academic Faculty

by

Timothy S. McPherson

In Partial Fulfillment
of the Requirements for the Degree
Master of Science in the
The George Woodruff School of Mechanical Engineering

Georgia Institute of Technology
August 2012

A FORCE AND DISPLACEMENT SELF-SENSING METHOD FOR A MRI COMPATIBLE TWEEZER END EFFECTOR

Approved by:

Jun Ueda, Advisor
Mechanical Engineering
Georgia Institute of Technology

Aldo Ferri
Mechanical Engineering
Georgia Institute of Technology

Alper Erturk
Mechanical Engineering
Georgia Institute of Technology

Date Approved: 22 June 2012

ACKNOWLEDGEMENTS

I wish to thank my Dr. Ueda, for his guidance and mentorship on this project. I have learned a great deal working in his lab. I am also indebted to my labmates, who have all helped me in many ways during my time here.

TABLE OF CONTENTS

LIST OF TABLES

LIST OF FIGURES

SUMMARY

This work describes a self-sensing technique for a piezoelectrically driven MRI-compatible tweezer style end effector, suitable for robot assisted, MRI guided surgery. Nested strain amplification mechanisms are used to amplify the displacement of the piezo actuators to practical levels for robotics. By using a hysteretic piezoelectric model and a two port network model for the compliant nested strain amplifiers, it is shown that force and displacement at the tweezer tip can be estimated if the input voltage and charge are measured. One piezo unit is used simultaneously as a sensor and an actuator, preserving the full actuation capability of the device. Experimental validation shows an average of 12% error between the self-sensed and true values.

CHAPTER I

INTRODUCTION

1.1 Motivation

Piezoelectric ceramics have been widely used in applications such as sound and ultrasound transduction, high voltage generation, and acceleration sensing [36]. As actuators, piezoceramics possess desirable qualities, such as high efficiency, high bandwidth, low noise, and no backlash. They have become widely used in micropostioning applications, most notably in atomic force microscopy [23]. Their small strain has limited their application in robotics. Most piezoelectric actuators generate on the order of micrometers of displacement. Recently, piezoelectrically driven devices have achieved strain of up to 20% by using "multi-layer nested rhombus" mechanisms that trade off force for displacement [35]. One such device, devloped by Kurita et. al., is a tweezer style end effector suitable for robotic surgery, and is the starting point of this research [24].

Robot assisted surgery has quickly become a highly active field of research and is beginning to enter mainstream medicine with the success of the Da Vinci robot, developed by Intuitive Surgical Inc. [12]. Concurrently, research has been undertaken in magnetic resonance imaging (MRI) guided surgery [29] [14] [17] [25]. The combination of these two fields has the potential to improve patient outcomes by reducing risk, and allowing an increasing number of procedures to be completed in a minimally invasive way. To that end, the investigation of new actuation and sensing strategies that are MRI compatible is needed to bring robotics into the MRI environment.

1.2 Research Objectives

This research will investigate a force and displacement self-sensing technique for a piezoelectrically driven tweezer style end-effector designed for use in robot assisted surgery. The device is driven by Lead Zirconate Titanate (PZT) actuators, a piezoelectric ceramic. Due to its ceramic nature it has low magnetic susceptibility, making it a good choice for use in MRI environments. A self-sensing design is desirable because it provides sensing without adding additional dedicated sensors, maintaining the MRI compatibility of the device and the full actuation capability. It also reduces the device's complexity and lowers its cost.

CHAPTER II

BACKGROUND AND LITERATURE REVIEW

2.1 MRI Compatible Robotics

Most traditional actuators and sensors make use of electromagnetic induction or ferromagnetic materials for their operation, and cannot be used in MRI environments. Accordingly, a number of strategies for MRI compatible actuation and sensing have been investigated in the literature, such as hydraulics, pneumatics, piezoelectricity, and electrostriction [33]. Kim et. al. used a saline based hydraulic system to assist in minimally invasive liver surgery [20]. The system had some drawbacks, including leakage and air bubbles. One of the most successful designs is the pneumatically powered step motor, PneuStep, developed by Stoianovici et. al. [30]. Due to it's stepping design it can achieve very precise motion. Additionally it is constructed completely from non-magnetic, non-conductive materials, producing very minimal image distortion. Another pneumatic robot was developed by Fischer et. al. for prostate needle placement, and makes use of custom designed MRI compatible pneumatic cylinders. One of the most popular actuator choices is piezoelectrically driven ultrasonic motors [6] [18], due to their small size and relatively high torque. Nearly all commercial piezoelectric actuators are ceramic materials, which do not interact significantly with magnetic fields. Piezoelectric actuators are also relatively high voltage devices which draw low current. Electrical currents can interact with MRI and degrade the image. However, in many cases the trade off for size and weight may be worth the decrease in image quality.

Many MRI compatible sensors have also been developed. One popular idea is the use of fiber optic cable for data transmission. In that vein, force sensors [32] [34] [31]

and encoders [6] have been proposed and investigated. Another strategy is using the MR image itself by placing markers on a device to track its location [9].

In this work a self-sensing technique will be developed so that a piezoelectric actuator driving the device can be used as a sensor simultaneously. This allows the device to remain compact and simple. It could also open the possibility of providing a remote surgeon with force feedback for MRI guided tele-surgery.

2.2 Piezoelectric Self-Sensing

Piezoelectric self-sensing was originally proposed by Dosch et. al. in [8]. A bridge circuit was developed by placing capacitances in series and parallel with the piezoelectric actuator that produced a voltage output proportional to velocity or force. The method was subsequently refined and applied by other researchers [10] [23]. The three main drawbacks of the method are that the operation of the bridge circuit requires close matching of the piezo capacitance, only dynamic measurements are possible, and a linear piezoelectric model is used. At the time these drawbacks were not too significant, but they have limited the method's applicability as applications for piezoelectric actuators have diversified to include quasistatic operation. Additionally, in many modern applications hysteresis is not negligible. More recent work has addressed some of these issues by developing methods based on charge measurement [15] [16] [27]. New models have also been developed to take hysteresis into account [13] [11]. One drawback of the previously cited charge measurement techniques is that they assume constant loading conditions, generally zero force or zero displacement, and none model hysteresis. As explained in [13], hysteresis is observed between voltage and charge but not charge and displacement, which suggests that the hysteresis occurs in the the electrical domain. This means that for quasistatic operation charge is linearly related to displacement if there is zero external force on the actuator, or vice versa, so the linear model can appear correct. If one attempts

to extend this model to a self-sensing scheme with unknown loading conditions, it is quickly seen that a model taking hysteresis into account is needed. Badel et. al. use the hysteretic model of [13] to achieve this, as well as implementing force control based on the self-sensed measurement [2].

Estimating the force and displacement at the endpoint of a compliant mechanism driven by piezoelectric actuators is a significantly more complicated problem. Kurita et. al. began to investigate this problem for a tweezer style end effector, and proposed using one actuator out of five solely as a sensor [24], their work also assumes either a blocked or free condition at the endpoint of the tweezer structure. Their results are promising, but in most applications knowledge of the loading condition at the tip will not be known a priori. Therefore a more sophisticated sensing technique is needed. Additionally, a self-sensing technique is attractive because it does not sacrifice actuation capability.

CHAPTER III

TWEEZER MECHANISM

3.1 Nested Strain Amplification

Piezoelectric actuators produce extremely small strain, in general on the order of 0.1%, but comparatively large force. For robotic applications, larger displacements can be achieved by trading off force with amplification mechanisms, such as the rhomboidal mechanism shown in Fig.1. By nesting several of such mechanisms inside

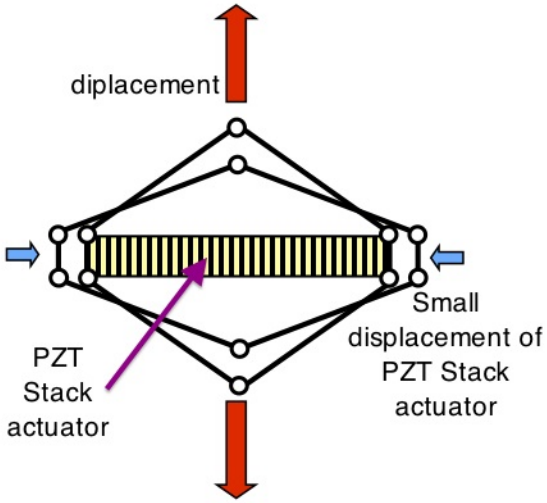

Figure 1: Idealized Rhomboidal Strain Amplification Mechanism

each other, strain rates of up to 20% can be achieved with sufficient force [35]. Using this princple, piezoelectrically driven tweezers were developed with three layers of strain amplification [24]. The first layer is made up of five commercially available Cedrat APA35XS piezoelectric actuators, seen in Fig.2. The APA35XS consists of a multilayer Lead Zirconate Titanate (PZT) stack actuator surrounded by a single rhomboidal strain amplifier. These actuators are surrounded by a second amplification mechanism, seen in Fig.3. Finally, the lever action of the tweezer arms themselves

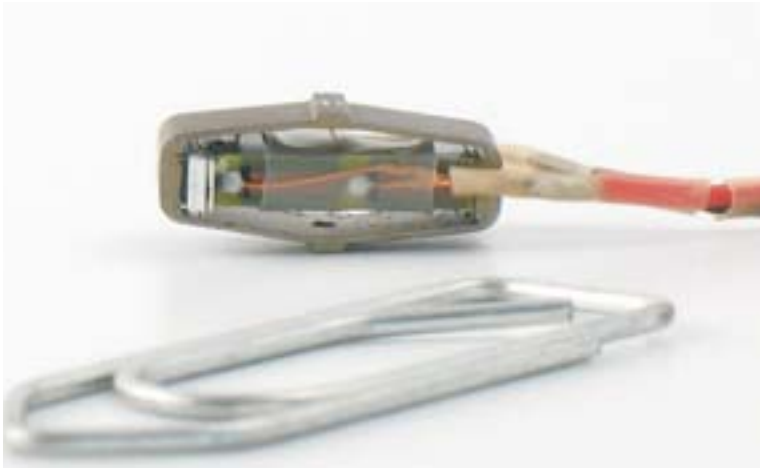

Figure 2: Cedrat APA35XS Actuator

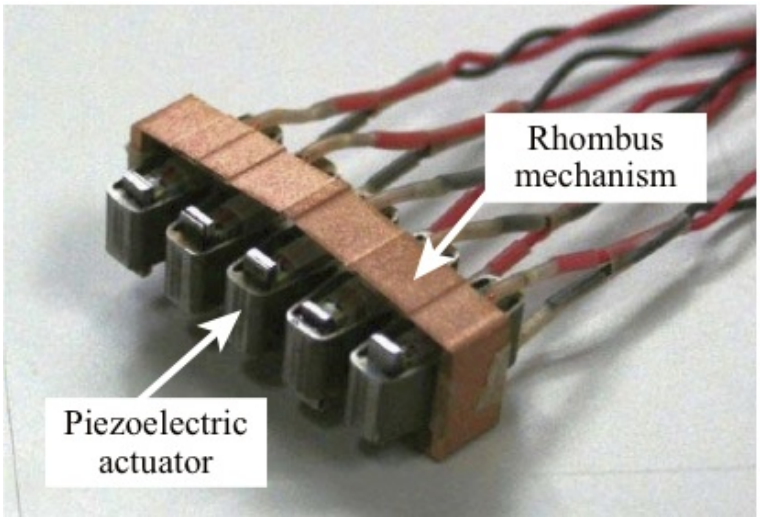

Figure 3: First and Second Amplification Layers

provide a third layer of amplification, shown in Fig. 4. The fully assembled tweezer device is shown in Fig.5. The tweezers produce 0.1 N of pinching force when fully blocked or 7 mm of displacement when fully free, and require a supply voltage of 0 to 150 V.

Under quasistatic operation, a rhomboidal strain amplifier can be represented using the lumped parameter model developed by Ueda, Secord, and Asada, shown in Fig.7 [35]. Based on the model, the following equations are obtained.

$$f_{pzt} + k_{BI}(\Delta x_c - \Delta x_{pzt}) - k_{pzt}\Delta x_{pzt} = 0 \tag{1}$$

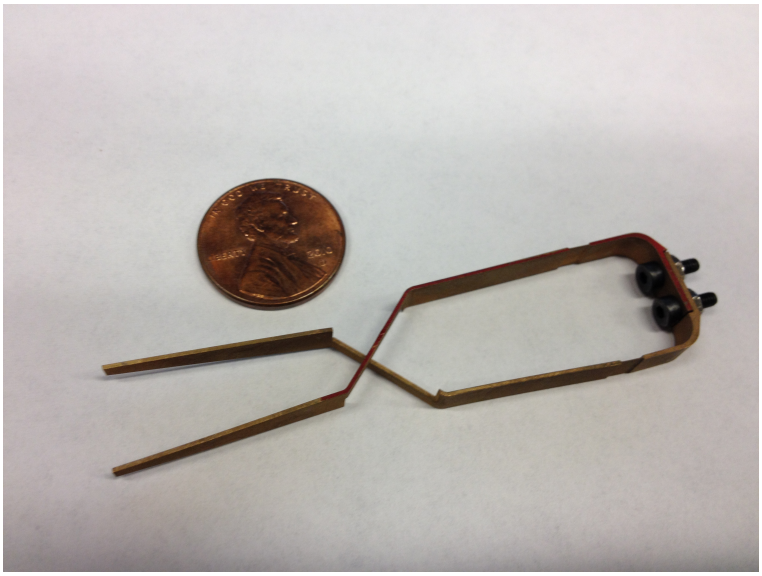

Figure 4: Tweezer arms, the third layer of amplification

$$ak_{BO}(a\Delta x_c - \Delta x_1) + k_J\Delta x_c + k_{BI}(\Delta x_c - \Delta x_{pzt}) = 0 \tag{2}$$

$$f_1 = k_{load}\Delta x_1 = k_{BO}(a\Delta x_c - \Delta x_1) \tag{3}$$

Note that Δx_c is an artifact of the model that has no physical meaning, while f_{pzt}, Δx_{pzt}, f_1, and Δx_1 are the input and output forces and displacements, as seen in Fig.6. Combining (2) and (3) we can solve for Δx_c:

$$\Delta x_c = \frac{ak_{BO}\Delta x_1 + k_{BI}\Delta x_{pzt}}{k_J + k_{BI} + a^2k_{BO}} \tag{4}$$

Also, define

$$f_{in} = f_{pzt} - k_{pzt}\Delta x_{pzt} \tag{5}$$

as the force applied by the PZT actuator to its environment. Then, (4) and (5) can be substituted into (1) and (3) to get f_1 and f_{in} solely in terms of Δx_1 and Δx_{pzt}.

$$f_{in} = \left(-k_{BI} + \frac{k_{BI}}{k_J + k_{BI} + a^2k_{BO}}\right)\Delta x_{pzt} + \left(\frac{ak_{BO}k_{BI}}{k_J + k_{BI} + a^2k_{BO}}\right)\Delta x_1 \tag{6}$$

$$f_1 = \left(\frac{ak_{BO}k_{BI}}{k_J + k_{BI} + a^2k_{BO}}\right)\Delta x_{pzt} + \left(\frac{k_{BO}^2a^2}{k_J + k_{BI} + a^2k_{BO}} - k_{BO}\right)\Delta x_1 \tag{7}$$

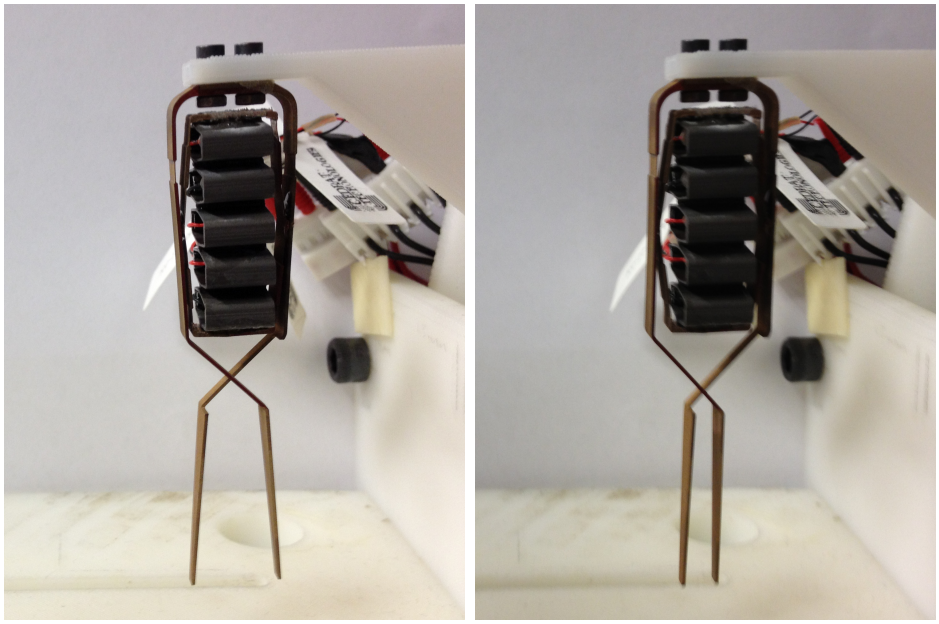

(a) Open (b) Closed

Figure 5: Fully assembled tweezer structure. The tweezers arms act as the third layer of amplification.

Equations (6) and (7) can be written equivalently as a matrix equation of the form

$$\begin{bmatrix} f_{pzt} \\ f_1 \end{bmatrix} = \begin{bmatrix} s_1 & s_3 \\ s_3 & s_2 \end{bmatrix} \begin{bmatrix} \Delta x_{pzt} \\ \Delta x_1 \end{bmatrix} \tag{8}$$

where

$$s_1 = -k_{BI} + \frac{k_{BI}}{k_J + k_{BI} + a^2 k_{BO}} \tag{9}$$

$$s_2 = \frac{k_{BO}^2 a^2}{k_J + k_{BI} + a^2 k_{BO}} - k_{BO} \tag{10}$$

$$s_3 = \frac{a k_{BO} k_{BI}}{k_J + k_{BI} + a^2 k_{BO}} \tag{11}$$

Written in this form, we see the model can be interpreted as a two port network. The parameters of the model can be interpreted intuitively as follows. s_1 is the stiffness at the input when the output is blocked. s_2 is the stiffness at the output when the input is blocked. Finally, s_3 is the ratio of force produced at the blocked output to a given input displacement. A second rhomboidal strain amplifier constitutes the

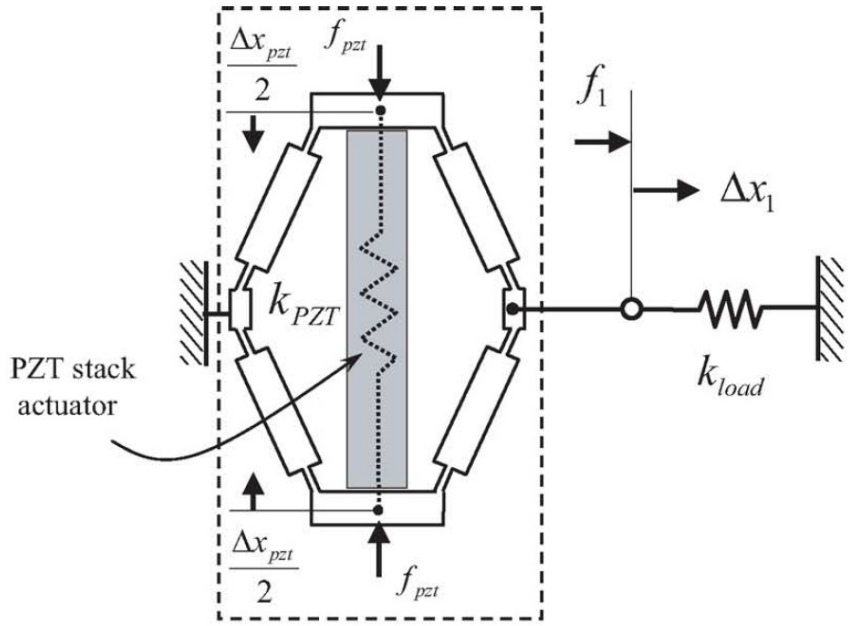

Figure 6: Schematic diagram of a rhomboidal strain amplifier

second amplification layer, seen in Fig. 8 and can be modeled similarly, where s_4,s_5, and s_6 are analogous to s_1,s_2, and s_3.

$$\begin{bmatrix} f_1 \\ f_2 \end{bmatrix} = \begin{bmatrix} s_4 & s_6 \\ s_6 & s_5 \end{bmatrix} \begin{bmatrix} \Delta x_1 \\ \Delta x_2 \end{bmatrix} \tag{12}$$

The lever action of the tweezer arms provide the final level of strain amplification. Figure 9 shows a schematic representation of the second and third layers. Assuming quasistatic operation, a two port network can also be written describing the third layer [24]

$$\begin{bmatrix} \Delta x_2 \\ \Delta x_{tip} \end{bmatrix} = \begin{bmatrix} Q_1 & Q_3 \\ Q_3 & Q_2 \end{bmatrix} \begin{bmatrix} f_2 \\ f_{tip} \end{bmatrix} \tag{13}$$

where

$$Q_1 = \left(\frac{C_{A2}}{2EI_1} + \frac{C_{A4}}{2EI_3} \right) \tag{14}$$

$$Q_3 = \left(\frac{C_{A1}}{2EI_1} + \frac{C_{A3}}{2EI_3} \right) \tag{15}$$

$$Q_2 = \left(\frac{C_{B1}}{2EI_1} + \frac{C_{B3}}{2EI_2} + \frac{C_{B4}}{2EI_3} \right) \tag{16}$$

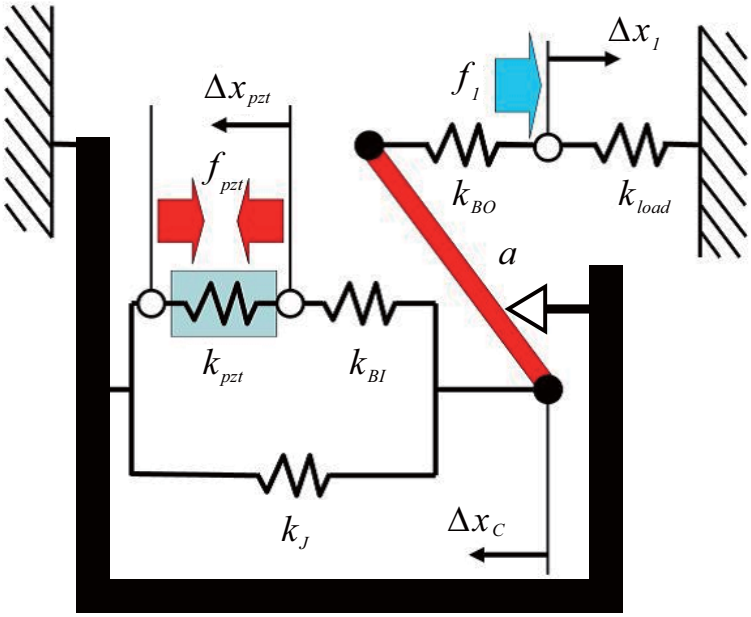

Figure 7: Schematic representation of the lumped parameter model for a rhomboidal strain amplifier.

E is the Young's Modulus of phosphor bronze, and I_1, I_2, and I_3 are the second moment of area. $C_{A1} \rightarrow C_{A4}$ and $C_{B1} \rightarrow C_{B5}$ are coefficients obtained using Castigliano's Theorem and the Bernoulli-Euler beam model [24].

The input-output behavior of nested rhomboidal strain amplifiers can be represented by single, combined two port network if every layer is represented by a two port network [35]. However, it is not immediately obvious how to account for the five actuators in series that drive the input of the second layer. The question arises, can five rhomboidal strain amplifiers connected in series also be represented by a single two port network model? If so, the input-output relationship of the tweezer mechanism as a whole could be assumed to be a two port network. Consider Fig. 10 and Fig. 11. We assume that each strain amplifier sees an identical input since the PZT actuators are connected electrically in parallel. When the output is blocked, we have the equivalent of five springs in parallel at the input, meaning the effective s_1 would be five times that of a single rhomboid. When the input is blocked, the rhomboids act as springs in series in the output direction, so the effective s_2 is one fifth that of a

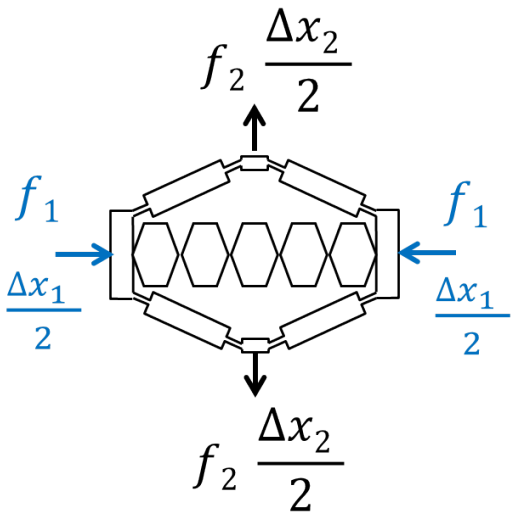

Figure 8: Schematic representation of second amplification layer. Note the five actuators in series that drive the input of the second layer

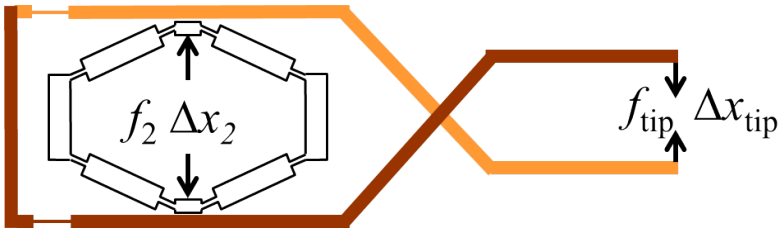

Figure 9: Schematic representation of the tweezer arms and second amplification layer

single rhomboid. Finally, when the output is blocked, a given input displacement will create the same output force for a singe rhombus as for five in series. The reaction forces at connection points cancel, leaving the output force unchanged. It is now seen that the series connection of five actuators can be modeled with a single two port network. The input force to the combined model is $5f_{in}$ and the input displacement is Δx_{pzt}, since the five PZT stack actuators act in parallel on the input.

Equation (8) can be rearranged to show outputs in terms of inputs, yielding

$$\begin{bmatrix} \Delta x_1 \\ f_1 \end{bmatrix} = \begin{bmatrix} \frac{-s_1}{s_3} & \frac{1}{s_3} \\ s_3 - \frac{s_1 s_2}{s_3} & \frac{s_2}{s_3} \end{bmatrix} \begin{bmatrix} \Delta x_{pzt} \\ f_{in} \end{bmatrix} \tag{17}$$

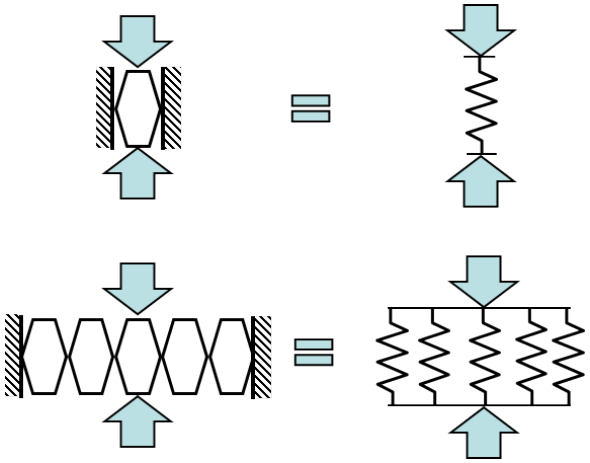

Figure 10: Mechanical analysis of five rhomboids in series, output blocked.

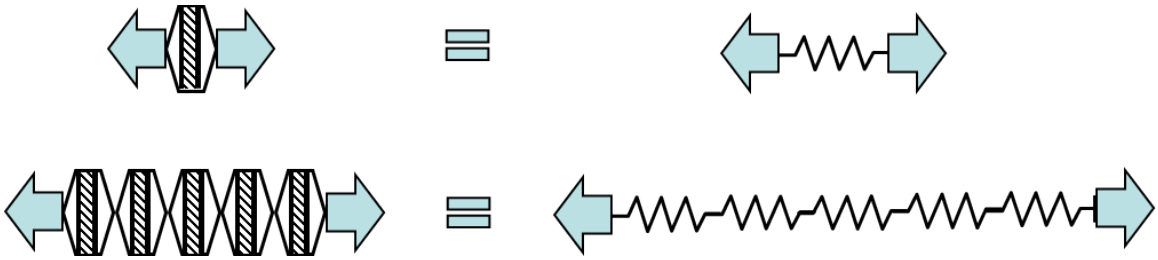

Figure 11: Mechanical analysis of five rhomboids in series, input blocked.

Similarly, (12) can be written as

$$\begin{bmatrix} \Delta x_2 \\ f_2 \end{bmatrix} = \begin{bmatrix} \dfrac{-s_4}{s_6} & \dfrac{1}{s_6} \\ s_6 - \dfrac{s_4 s_5}{s_6} & \dfrac{s_5}{s_6} \end{bmatrix} \begin{bmatrix} \Delta x_1 \\ f_1 \end{bmatrix} \tag{18}$$

and (13) as

$$\begin{bmatrix} \Delta x_{tip} \\ f_{tip} \end{bmatrix} = \begin{bmatrix} \dfrac{-Q_1}{Q_3} & \dfrac{1}{Q_3} \\ Q_3 - \dfrac{Q_1 Q_2}{Q_3} & \dfrac{Q_2}{Q_3} \end{bmatrix} \begin{bmatrix} \Delta x_2 \\ f_2 \end{bmatrix} \tag{19}$$

Equations (17), (18), and (19) can now be combined to give f_{tip} and Δx_{tip} in terms of f_{in} and Δx_{pzt}

$$\begin{bmatrix} \Delta x_{tip} \\ f_{in} \end{bmatrix} = \begin{bmatrix} \dfrac{-Q_1}{Q_3} & \dfrac{1}{Q_3} \\ Q_3 - \dfrac{Q_1 Q_2}{Q_3} & \dfrac{Q_2}{Q_3} \end{bmatrix} \begin{bmatrix} \dfrac{-s_4}{s_6} & \dfrac{1}{s_6} \\ s_6 - \dfrac{s_4 s_5}{s_6} & \dfrac{s_5}{s_6} \end{bmatrix} \begin{bmatrix} \dfrac{-n_A s_1}{s_3} & \dfrac{1}{s_3} \\ s_3 - \dfrac{s_1 s_2}{s_3} & \dfrac{s_2}{n_A s_3} \end{bmatrix} \begin{bmatrix} \Delta x_{pzt} \\ n_A f_{in} \end{bmatrix} \tag{20}$$

Note that the first layer matrix and input vector have been written in terms of a single rhomboid and PZT actuator, but the s-parameters and input force been appropriately modified as discussed above. n_A is the number of actuators connected in series, five in this case. Equivalently, we can write

$$\begin{bmatrix} \Delta x_{tip} \\ f_{tip} \end{bmatrix} = \begin{bmatrix} \frac{-S_1}{S_3} & \frac{1}{S_3} \\ S_3 - \frac{S_1 S_2}{S_3} & \frac{S_2}{S_3} \end{bmatrix} \begin{bmatrix} \Delta x_{pzt} \\ n_A f_{in} \end{bmatrix} \tag{21}$$

where S_1,S_2, and S_3 are the parameters describing the combined effects of all three amplification layers.

3.2 Material Selection

To ensure MRI compatibility the device must be constructed materials of sufficiently low magnetic susceptibility. As a ceramic, PZT is relatively unaffected by magnetic fields. The metal amplification structure of the Cedrat APA35XS actuators are titanium. This is a non-standard option, but is readily available from the manufacturer. The tweezer structure itself is machined from phosphor bronze. Both titanium and phosphor bronze have relatively low magnetic susceptibility and are considered safe to use in MRI environments [28].

MRI compatibility encompasses two main ideas. First, the device should experience forces and torques within the MRI chamber that are low enough to be negligible. Second, the imaging should be degraded as little as possible [28]. A static test was performed to asses the MRI compatibility of the device. As expected, the device was not significantly affected by the magnetic fields. The effect on the image quality is shown in Fig. 12. The images show a round ball in the MRI chamber. The tweezers create slight distortion of the image. Additionally the signal to noise ratio of the image is lowered slightly from 22.84 to 21.08. In general the image distortion is not severe. Though only a static test was performed, piezoelectrically driven devices constructed of titanium have been tested by Cedrat and were shown to produce acceptable levels

of image distortion [4]. Other studies have also shown piezoelectrically driven actuators will produce low levels of noise and distortion with appropriate shielding of the driving electronics [7] [37]. This indicates that the device could be used in the MRI environment.

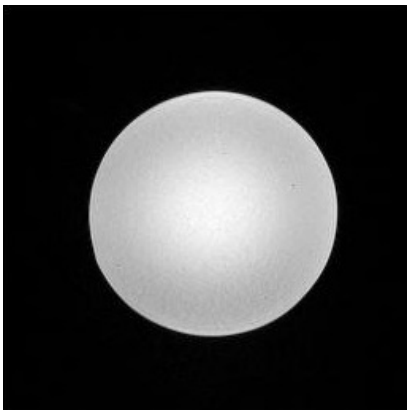

(a) Reference

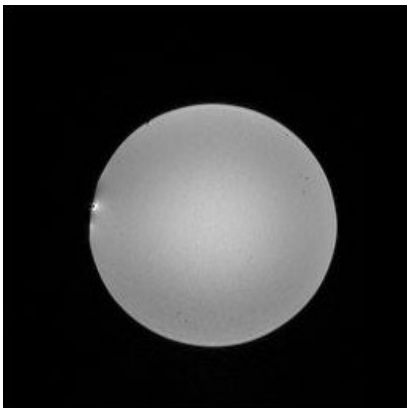

(b) Tweezer Device in Chamber

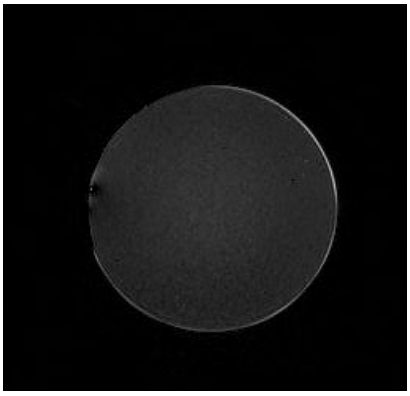

(c) Difference between reference and tweezer test

Figure 12: Effect of tweezers on image MRI image quality

CHAPTER IV

SIMULTANEOUS FORCE AND DISPLACEMENT SELF-SENSING

4.1 Electromechanical Modeling of Piezoelectric Actuators

Piezoelectric materials have crystal structures such that an electric field is generated by mechanical deformation. Conversely, an applied electric field will cause a mechanical deformation. These effects are known as the direct and converse piezoelectric effects [19]. One of the most widely used models for piezoelectric actuators come from IEEE Standard 176. The electromechanical coupling is described in tensor notation by (22) and (23) [19]

$$D_i = \epsilon_{ij}^T E_j + d_{ijk} T_{jk} \tag{22}$$

$$S_{ij} = \underline{\mathrm{d}}_{ijk} E_k + s_{ijkl}^E T_{kl} \tag{23}$$

where D_i is electric displacement, ϵ is permittivity, E is electric field, T is stress, S is strain, s is compliance, and d_{ijk} and $\underline{\mathrm{d}}_{ijk}$ are the piezoelectric constants. Electric displacement and strain are assumed to be linearly dependent on electric field strength and stress. However, the range in which the linear model is accurate is quite small, as piezoceramics are known to exhibit pronounced hysteresis. Subsequently, more complex models have been developed, such as the one proposed by Goldfarb and Celanovic that is now widely in use [13]. Since significant hysteresis has been observed in the piezoelectrically driven tweezers, this model will be used rather than the simpler linear model.

A schematic representation of the model is shown in Fig. 13. The model describes the hysteric behavior of the actuator in addition to the electrical-mechanical interplay

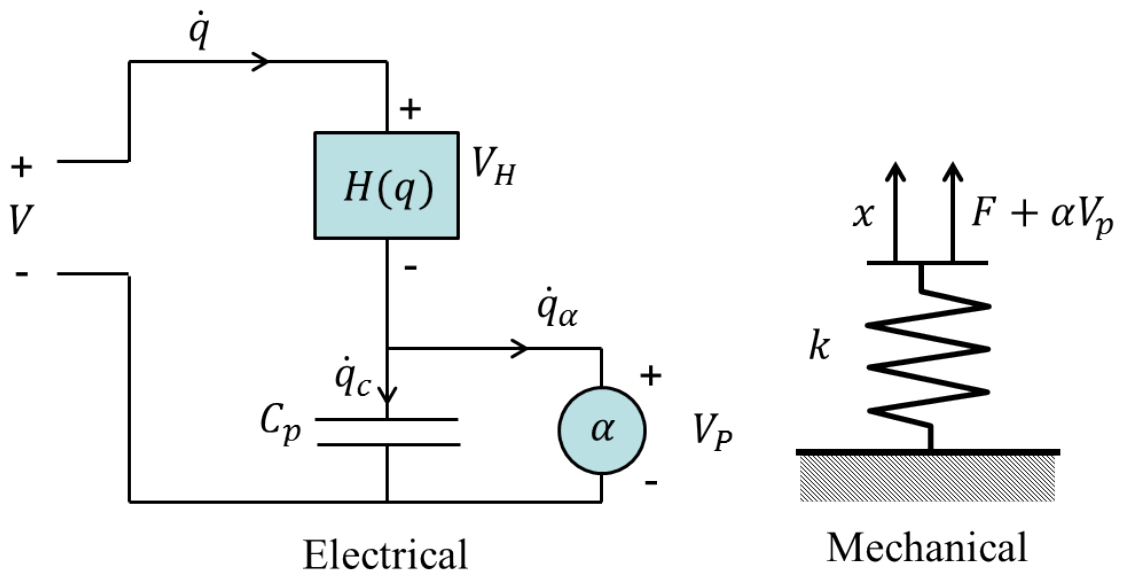

Figure 13: Piezoelectric Actuator Model

caused the the direct and converse piezoelectric effects. The model is described by (24) through (27).

$$q = \alpha x + C_p V_p \tag{24}$$

$$V_H = H(q) \tag{25}$$

$$\frac{x}{F + \alpha V_p} = \frac{1}{k} \tag{26}$$

$$V = V_p + V_H \tag{27}$$

q is electric charge, V is the input voltage supplied to the actuator, α is the transformer ratio of the actuator with units of $^{\mathrm{N}}/_{\mathrm{V}}$, C_p is the clamped capacitance of the actuator, F is the external force, and k is the short circuit stiffness of the actuator. $H(q)$ is a hysteresis operator whose form will be discussed in the following section.

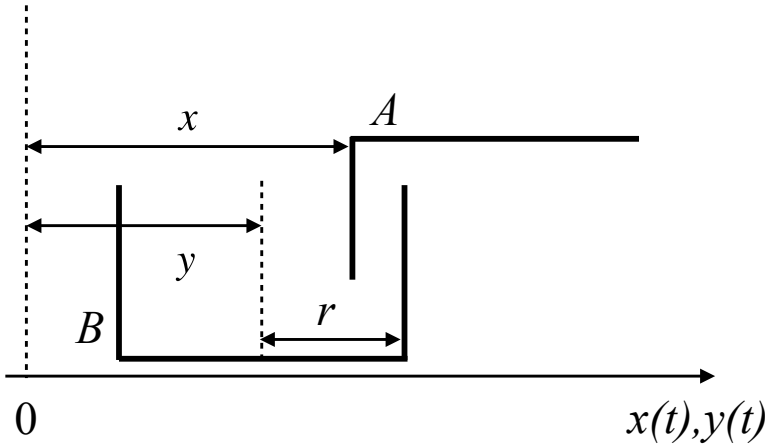

Figure 14: Schematic representation of the play operator

4.2 Hysteresis Modeling

4.2.1 The Modified Prandtl-Ishlinskii Hysteresis Model

Many phenomenological models are available for modeling hysteresis, such as the Prandtl-Ishlinskii operator [21], Preisach operator [5], Generalized Maxwell Slip Operator [13], and differential equations method [3]. Here, the modified Prandtl-Ishlinkii approach developed by Kuhnen will be used [22]. It has several useful advantages, such as the ability to model asymmetric loops and minor loops, an automatic identification procedure, and extendability to creep modeling.

In general the Prandtl-Ishlinskii operator is defined as

$$y(t) = \int_0^\infty p(r) H_{r_H}[x, y_0](t) dr \tag{28}$$

where $p(r)$ is a density function and $H_{r_H}[x, y_0](t)$ is the play operator. A schematic representation of the play operator is shown in Fig. 14. The input is the position of element A and the output is the position of element B. r is the threshold value that characterizes the operator. Such a system will display a simple, rate independent hysteresis between input and output, shown in Fig. 15. Mathematically, the play operator can be represented recursively by

$$y(t_0) = H(x(t_0), y_0, r_H) \tag{29}$$

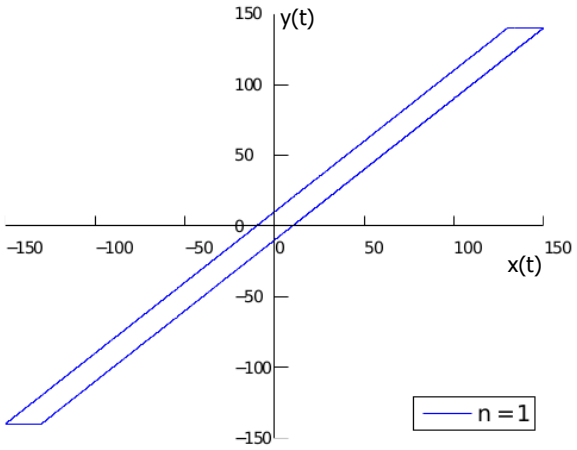

Figure 15: The simple hysteretic behavior of the play operator

$$y(t) = H_{r_H}[x, y_0](t) = H(x(t), y(t_i), r_H) \quad \text{for} \quad t_i < t \leq t_{i+1}, \quad 0 \leq i \leq N-1 \tag{30}$$

for given initial time t_0, initial output position y_0, and monotonicity partition $t_0 < t_1 < \cdots < t_N$ such that the input x is monotonic on every $[t_i, t_{i+1}]$ [5]. H is defined as

$$H(x, y, r_H) = \max(x - r_H, \min(x + r_H, y)) \tag{31}$$

which describes a sliding symmetric dead zone. r_H is the threshold of the dead zone, analogous to width of element B in Fig. 14.

Equation (28) represents the linear superposition of an infinite number of play operators with thresholds varying from 0 to ∞, and can model more complex hysteresis loops than that shown in Fig. 15. In practice, this can be approximated by the weighted sum of a finite number of play operators, which is expressed as the product

$$H[x](t) := \boldsymbol{w}_H^T \cdot \boldsymbol{H}_{\boldsymbol{r}_H}[x, \boldsymbol{z}_{H0}](t) \tag{32}$$

where $\boldsymbol{w}_H^T = [w_{H0}\ w_{H1} \cdots w_{Hn}]$ is a vector of weights, $\boldsymbol{r}_H^T = [r_{H0}\ r_{H1} \cdots r_{Hn}]$ is a vector of threshold values, $\boldsymbol{z}_{H0}^T = [z_{H00}\ z_{H01} \cdots z_{H0n}]$ is a vector of initial conditions, and $\boldsymbol{H}_{\boldsymbol{r}_H}[x, \boldsymbol{z}_{H0}](t)^T = [H_{r_{H0}}[x, z_{H00}](t)\ H_{r_{H1}}[x, z_{H01}](t) \cdots H_{r_{Hn}}[x, z_{H0n}](t)]$ is a vector of play operators. The threshold values are subject to $0 = r_{H0} < r_{H1} < \cdots < r_{Hn} < \infty$.

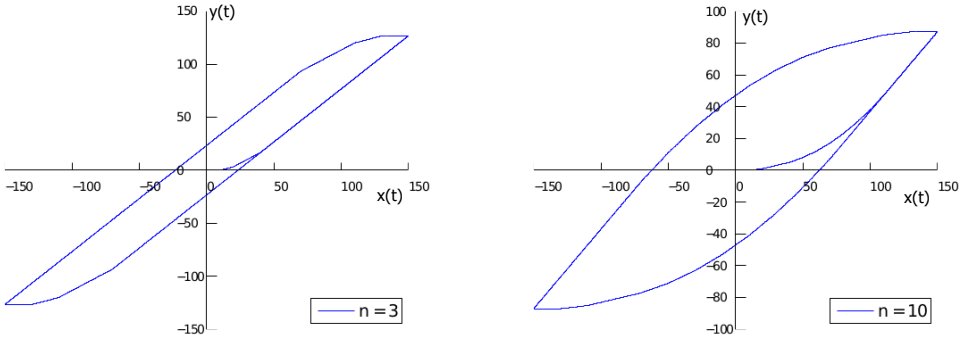

(a) Superposition of three play operators (b) Superposition of ten play operators

Figure 16: Summation of play operators

Figure 16 shows how play operators combine to form a more complex hyster

This formulation can only model symmetric hysteresis loops, but the introduction of a memory free superposition operator allows asymmetric loops to be modeled [21]. The superposition operator is defined by a one sided dead zone function

$$y(t) = S_{r_S}[x](t) = \begin{cases} \max(x(t) - r_s, 0) & \text{if } r_s > 0 \\ x(t) & \text{if } r_s = 0 \\ \min(x(t) - r_s) & \text{if } r_s < 0 \end{cases} \tag{33}$$

where r_S is the threshold value of the dead zone. In this application the input is the charge on the PZT actuator, which is assumed to be nonnegative since the applied voltage is always nonnegative. Therefore for this case we can simplify (33) to

$$y(t) = S_{r_S}[x](t) = \max(x(t) - r_s, 0) \tag{34}$$

In a similar fashion to (32) a finite number of superposition operators can be summed to model more complex behavior.

$$S[x](t) := \boldsymbol{w}_S^T \cdot \boldsymbol{S}_{\boldsymbol{r}_S}[x](t) \tag{35}$$

$\boldsymbol{w}_S^T = [w_{S0}\ w_{S1} \cdots w_{Sl}]$ is the vector of weights and $\boldsymbol{r}_S^T = [r_{S0}\ r_{S1} \cdots r_{Sl}]$ is the vector of

thresholds, subject to $r_{S0} = 0 < r_{S1} < \cdots < r_{Sl} < \infty$. The modified discrete Prandtl-Ishlinksii operator combines the play and superposition operators and is defined as

$$\Gamma[x](t) := \boldsymbol{w}_S^T \cdot \boldsymbol{S}_{\boldsymbol{r}_S}[\boldsymbol{w}_H^T \cdot \boldsymbol{H}_{\boldsymbol{r}_H}[x, \boldsymbol{z}_{H0}]](t) \tag{36}$$

As shown in [21], the operator can model asymmetric loops.

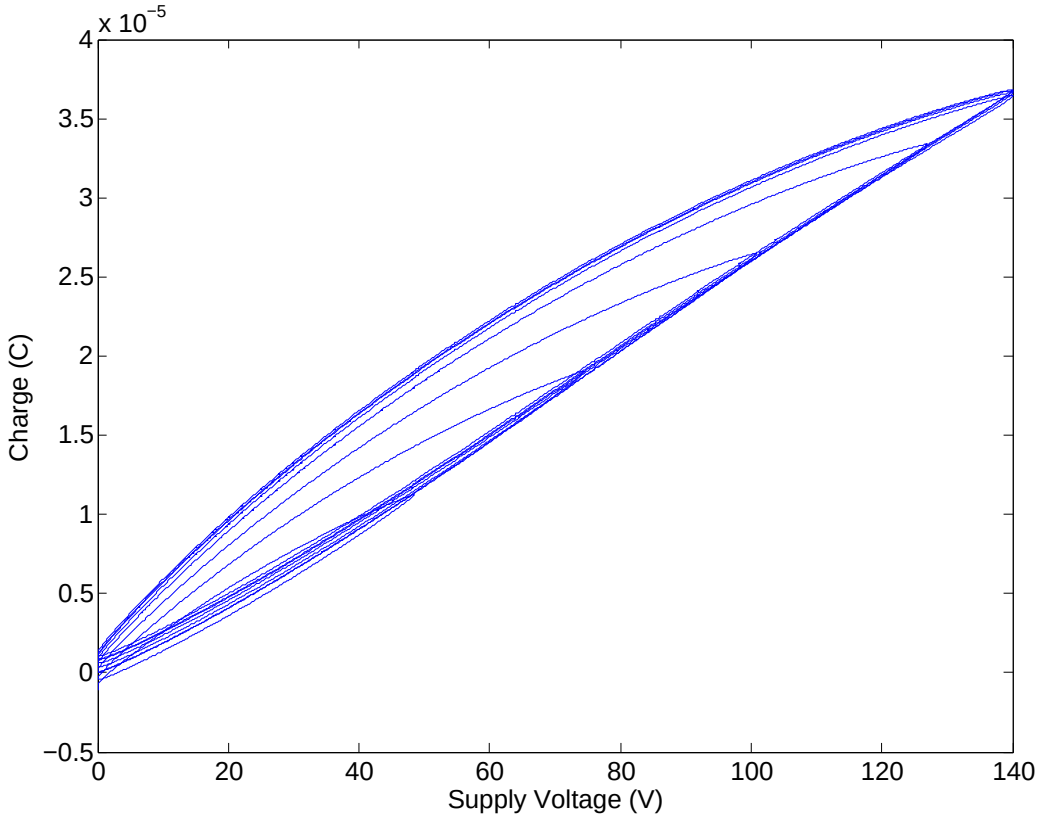

Figure 17: Hysteresis between input voltage and charge

Figure 17 shows that in addition to hysteresis there is also creep between voltage and charge. The modified Prantdl-Ishlinskii operator can be extended to model this phenomenon as well with the addition of a creep operator that models the creep effect as $\log(t)$-type creep with a hysteretic equilibrium state [22]. The elementary creep operator is written as

$$y(t) = K_{r_K a_K}[x, y_{K0}](t) \tag{37}$$

and it is defined as the solution to the differential equation

$$\frac{d}{dt}y(t) = a_K \max(x(t) - y(t) - r_K, \min(x(t) - y(t) + r_K, 0)) \tag{38}$$

Though this definition is somewhat abstruse, (38) can be easily solved numerically. Using a zero order hold to approximate the integral, it's numerical solution takes the form

$$y_k = \begin{cases} e^{-a_K T_s} y_{k-1} + (1 - e^{-a_K T_s})(x_{k-1} - r_K) & \text{if } x_{k-1} - y_{k-1} \geq r_K \\ e^{-a_K T_s} y_{k-1} + (1 - e^{-a_K T_s})(x_{k-1} + r_K) & \text{if } x_{k-1} - y_{k-1} \leq -r_K \\ y_{k-1} & \text{if } -r_K < x_{k-1} - y_{k-1} < r_K \end{cases} \tag{39}$$

T_s is the sampling time, r_K is the threshold, a_K is called the creep eigenvalue. $\log(t)$-type creep refers to creep behavior that has a linear step response when viewed with respect to a logarithmic time scale. The summation of elementary creep operators produces this behavior when the creep eigenvalues are

$$a_{K_j} = \frac{1}{10^{j-1} T_s} \quad \text{for } j = 1, 2, \cdots, m \tag{40}$$

and is called the $\log(t)$-type creep operator [22]. As before, a finite number of $\log(t)$-type creep operators will be summed, giving

$$K[x](t) := \boldsymbol{w}_K^T \cdot \boldsymbol{K}_{\boldsymbol{r}_K \boldsymbol{a}_K}[x, \boldsymbol{Z}_{K0}](t) \cdot \boldsymbol{i} \tag{41}$$

where i is a $n \times 1$ vector of ones, $\boldsymbol{w}_K^T = [w_{K0}\ w_{K1} \ldots w_{Kn}]$ is a vector of weights, $\boldsymbol{r}_K^T = [r_{K0}\ r_{K1} \cdots r_{Kn}]$ is a vector of thresholds subject to $0 = r_{K0} < r_{K1} < \cdots < r_{Kn} < \infty$, and $\boldsymbol{a}_K = [a_{K1} \cdots a_{Km}]$ is the vector of creep eigenvalues according to (40). $\boldsymbol{K}_{\boldsymbol{r}_K \boldsymbol{a}_K}[x, \boldsymbol{Z}_{K0}](t)$ is a matrix of elementary creep operators, one for each combination of creep eigenvalue and threshold, shown below.

$$\boldsymbol{K}_{\boldsymbol{r}_K \boldsymbol{a}_K}[x, \boldsymbol{Z}_{K0}] = \begin{bmatrix} K_{r_{K0} a_{K1}}[x, z_{K001}] & \cdots & K_{r_{K0} a_{Km}}[x, z_{K00m}] \\ K_{r_{K1} a_{K1}}[x, z_{K011}] & \cdots & K_{r_{K1} a_{Km}}[x, z_{K01m}] \\ \vdots & \ddots & \vdots \\ K_{r_{Kn} a_{K1}}[x, z_{K0n1}] & \cdots & K_{r_{Kn} a_{Km}}[x, z_{K0nm}] \end{bmatrix}$$

Similarly, $\boldsymbol{Z}_{K0}$ is a matrix of initial conditions corresponding to each elementary creep operator.

$$\boldsymbol{Z}_{K0} = \begin{bmatrix} z_{K001} & \cdots & z_{K00m} \\ z_{K011} & \cdots & z_{K01m} \\ \vdots & \ddots & \vdots \\ z_{K0n1} & \cdots & z_{K0nm} \end{bmatrix}$$

Now, a combined hysteresis model is formed by adding the creep operator the the hysteresis operator in (36)

$$\Gamma[x](t) := \boldsymbol{w}_S^T \cdot \boldsymbol{S}_{\boldsymbol{r}_S}[\boldsymbol{w}_H^T \cdot \boldsymbol{H}_{\boldsymbol{r}_H}[x, \boldsymbol{z}_{H0}] + \boldsymbol{w}_K^T \cdot \boldsymbol{K}_{\boldsymbol{r}_K \boldsymbol{a}_K}[x, \boldsymbol{Z}_{K0}] \cdot \boldsymbol{i}](t) \tag{42}$$

This operator will be used as $H(q)$ in (25), so we have

$$V_H = H(q) = \Gamma[q](t) \tag{43}$$

4.2.2 Model Identification

One drawback of the modified Prandtl-Ishlinskii approach is the relatively large number of parameters that characterize the model. However, by making certain assumptions about the threshold values, the identification of the weights can be formulated as a quadratic programming problem [22]. This process is described in Appendix A. In short, one experiment is required to generate an input-output relationship. The weights are then optimized by a numerical search such that they minimize the error squared between model and experiment.

4.3 Self-Sensing Technique

4.3.1 Combined Electromechanical Model of the Tweezer Device

Equations (24) and (26) can be written in matrix form, shown in (44).

$$\begin{bmatrix} x \\ F \end{bmatrix} = \begin{bmatrix} \frac{1}{\alpha} & \frac{-C_p}{\alpha} \\ \frac{-k}{\alpha} & \alpha + \frac{C_p k}{\alpha} \end{bmatrix} \begin{bmatrix} q \\ V_p \end{bmatrix} \tag{44}$$

Note we have negated F since we wish to represent the force supplied by the PZT actuator rather than the external force on the actuator, since the latter is the input to the two port network model representing the tweezers. Combining (44) with (21) the force and displacement at the tip can be written in terms of q and V_p.

$$\begin{aligned}\begin{bmatrix}\Delta x_{tip}\\ f_{tip}\end{bmatrix} &= \begin{bmatrix}\dfrac{-S_1}{S_3} & \dfrac{1}{S_3}\\ S_3-\dfrac{S_1S_2}{S_3} & \dfrac{S_2}{S_3}\end{bmatrix}\begin{bmatrix}\dfrac{1}{n_A\alpha} & \dfrac{-C_p}{\alpha}\\ \dfrac{-k}{\alpha} & n_A\alpha+\dfrac{n_AC_pk}{\alpha}\end{bmatrix}\begin{bmatrix}n_Aq\\ V_p\end{bmatrix}\\ &= \begin{bmatrix}\dfrac{-n_Ak-S_1}{n_AS_3\alpha} & \dfrac{n_AC_pk+C_pS_1+n_A\alpha^2}{S_3\alpha}\\ \dfrac{S_2(-n_Ak-S_1)+S_3^2}{n_AS_3\alpha} & \dfrac{S_2(n_AC_pk+C_pS_1+n_A\alpha^2)-CpS_3^2}{S_3\alpha}\end{bmatrix}\begin{bmatrix}n_Aq\\ V_p\end{bmatrix}\end{aligned} \tag{45}$$

Note that the matrix of (44) has been modified to reflect that connection of actuators electrically in parallel, but constants α, C_p, and k are with respect to a single actuator. For n_A actuators connected in parallel, α, C_p, and k will all increase by a factor of n_A, which is reflected in (45). Additionally the charge will be n_A times that of a single actuator. As described earlier, here n_A is five. By noticing the similarity between the first and second rows of the matrix, (45) can be expressed as

$$\begin{bmatrix}\Delta x_{tip}\\ f_{tip}\end{bmatrix} = \begin{bmatrix}A_1 & A_2\\ S_2A_1+S_3/n_A\alpha & S_2A_2-C_pS_3/\alpha\end{bmatrix}\begin{bmatrix}n_Aq\\ V_p\end{bmatrix} \tag{46}$$

where A_1 and A_2 are defined by

$$A_1 = \frac{-n_Ak-S_1}{n_AS_3\alpha} \tag{47}$$

$$A_2 = \frac{n_AC_pk+C_pS_1+n_A\alpha^2}{S_3\alpha} \tag{48}$$

Recalling that $V_p = V - H(q)$, It is now seen that the force and displacement at the tweezer tip can be sensed simultaneously if the driving voltage, charge, and hysteresis operator $H(q)$ are known.

4.3.2 Model Parameter Identification

In prior work on piezoelectric modeling and self-sensing, identification of model parameters has been relatively straightforward [13] [2]. However, the addition of strain amplification mechanisms complicates the matter. For a singular, unamplified PZT actuator, the parameters α, k, and C_p, and the hysteresis operator $H(q)$ can be identified by taking three measurements, namely the maximum force generated by the blocked actuator, the maximum displacement of the free actuator, and the charge vs. voltage profile of the free actuator as the input voltage is varied from it's minimum to maximum value [2]. When the PZT actuator is nested inside several layers of strain amplification, it is impossible to recreate the necessary loading conditions. Since the PZT actuator and first layer strain amplifier come together as a commercially available unit, the PZT actuator cannot be removed and evaluated separately. The s-paramters of each layer could be identified as described in [35], but the same problem prevents the paramters of the first layer from being measured. However, even if these approaches were possible, it would be undesirable to require disassembly of the device for model calibration. The form of (46) hints at the solution to this problem.

The parameters S_1, S_2, and S_3 can be estimated by the following equations [35].

$$S_1 = \frac{f_{in}^{block}}{\Delta x_{pzt}^{block}} \tag{49}$$

$$S_2 = \frac{\Delta x_{tip}^{free}}{\Delta x_{pzt}^{free}} \frac{\Delta x_{pzt}^{block}}{f_{tip}^{block}} \tag{50}$$

$$S_3 = -\frac{f_{tip}^{block}}{\Delta x_{pzt}^{block}} \tag{51}$$

Recall f_{in} and Δx_{pzt} are the input force and displacement supplied by the PZT actuator, while f_{tip} and Δx_{tip} are the force and displacement at the tweezer tip.The superscript *block* or *free* indicates the loading condition at the tweezer tip when the measurement is taken. As discussed above, f_{tip} and Δx_{tip} can be measured easily, while f_{in} and Δx_{pzt} cannot. However, based on catalog data f_{in} and Δx_{pzt} can be

Table 1: Cedrat MLA 2510 Piezoelectric Actuator Properties

Free Displacement	10 μm
Blocked Force	240 N
Stiffness	24 N/μm
Capacitance	0.25 μF
Maximum Driving Voltage	150 V

Table 2: Actuator Parameter Estimates Based on Catalog Data

(a)

Actuator Measurement Guesses	
Δx_{tip}^{free}	6.4 mm
Δx_{pzt}^{free}	7 μm
Δx_{pzt}^{block}	5 μm
f_{in}^{block}	200 N
f_{tip}^{block}	0.1 N

(b)

Model Parameters	
S_1	2×10^8 N/m
S_2	$4.5 \times 10^{-}3$ N/m
S_3	-2×10^5 N/m
α	1.6 N/V
k	24 N/μm
C_p	.25 μF

(c)

Eq. 46 terms	
A_1	-1000
A_2	$1.7 \times 10^{-}3$
S_2A_1	45.7
S_2A_2	$7.5 \times 10^{-}5$
$S_3/5\alpha$	-2500
C_pS_3/α	$3.1 \times 10^{-}3$

assumed to fall within certain ranges. Table 1 shows the published values for the Cedrat MLA 2510, which is the piezoelectric actuator inside the Cedrat APA35XS amplified actuators that are used in the tweezer device [1]. The values can be used to get an idea of the relative order of magnitude of the terms in (46). Based on the information in Table 1, guesses can be made for measurements needed in (49), (50), and (51) shown in Table 2(a). S_1, S_2, and S_3 can then be estimated as well as the parameters of the piezoelectric model, shown in Table 2(b). Based on Table 2(b), the terms of (46) can be calculated, which allows their relative orders of magnitude to be compared. These are displayed in Table 2(c). Now, we examine the term $S_2A_1 + S_3/5\alpha$. The term S_2A_1 is two orders of magnitude smaller than $S_3/5\alpha$. Similarly,

the term $S_2A_2 - C_pS_3/\alpha$ is examined. S_2A_2 is two orders of magnitude smaller than C_pS_3/α. Based on this insight, we can safely approximate (46) as follows.

$$\begin{bmatrix} \Delta x_{tip} \\ f_{tip} \end{bmatrix} = \begin{bmatrix} A_1 & A_2 \\ A_3/n_A & -C_pA_3 \end{bmatrix} \begin{bmatrix} n_Aq \\ V_p \end{bmatrix} \tag{52}$$

$$A_3 = \frac{S_3}{\alpha} \tag{53}$$

This approximation is useful because it allows the hysteresis operator $H(q)$ to be calibrated without knowledge of A_1, A_2, or A_3. When the tip is free, i.e. $f_{tip} \equiv 0$, we can write

$$q = C_pV_p \tag{54}$$

The approximation of used in (52) has allowed the term A_3 to cancel. Combining (54) with (25) and (27) gives

$$H(q) = V - \frac{q}{C_p} \tag{55}$$

Therefore only knowledge of C_p is required to calibrate $H(q)$. Once $H(q)$ is known, A_1, A_2, and A_3 can be easily determined by regression.

CHAPTER V

EXPERIMENTAL VALIDATION

5.1 Hardware and Setup

5.1.1 Charge and Voltage Measurement

The inputs to the sensing model are charge and voltage. The actuators are driven by a Cedrat CA45 high voltage amplifier. The amplifier shows good linearity up to 500 Hz, well above the quasistatic operation considered here. This means that in practice the supply voltage does not need to be measured directly, but can assumed to be the amplifier gain times the input voltage to the amp. This eliminates the need for high voltage measurement equipment. The voltage across the actuator is given by

$$V = V_c - V_s \tag{56}$$

Charge can be accurately measured by placing a shunt resistance in series with a PZT actuator and measuring the voltage drop across it [2]. The charge is then calculated by integrating the current over time.

$$q(t) = \frac{1}{R}\int_0^t V_s d\tau \tag{57}$$

$q(t)$ is the charge on the PZT actuator at time t, R is the shunt resistance, and v_s is the measured voltage across the resistance. Figure 18 shows the circuit used to measure charge. V is the driving voltage from the amplifier and R is the shunt resistance. An instrumentation amp measures the voltage drop across the shunt resistor. An instrumentation amp measures a differential voltage with a high impedance input on both the positive and negative terminals and low impedance at the output. This ensures minimal interaction between data acquisition hardware and the PZT actuators. It also ensures that the data acquisition hardware measures a low impedance source,

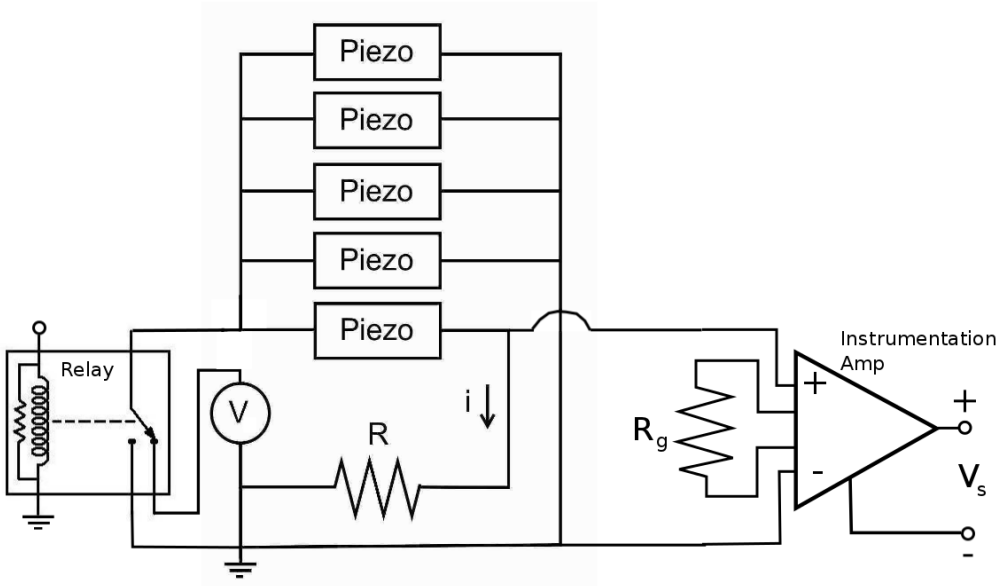

Figure 18: Charge Measurement Circuit

which will give the best accuracy [26]. The relay allows the leads of the PZT actuators to be shorted to ground. Hysteresis is dependent on initial conditions [5]. Shorting the leads allows a consistent initial condition to be established so that hysteresis modeling will be more accurate.

5.1.2 Experimental Setup

To assess the force and displacement self-sensing two experimental setups are used. Though the self-sensing technique can estimate force and displacement simultaneously, they are evaluated separately here because it simplifies taking the reference measurement. For displacement, a Micro-Epsilon OptoNCDT 1300 Laser Displacement sensor with a range of 20 mm and resolution of 4 μm is used as a reference measurement. The experimental setup is shown in Fig. 19 To measure the force at the tip a Futek LSB200 load cell with a range of 1 N and 0.1% accuracy of is used, with an Omega DRG-SC-BG signal conditioner. The experimental setup is shown in Fig. 20 For both cases a National Instruments USB 6229 was used to measure V_s and

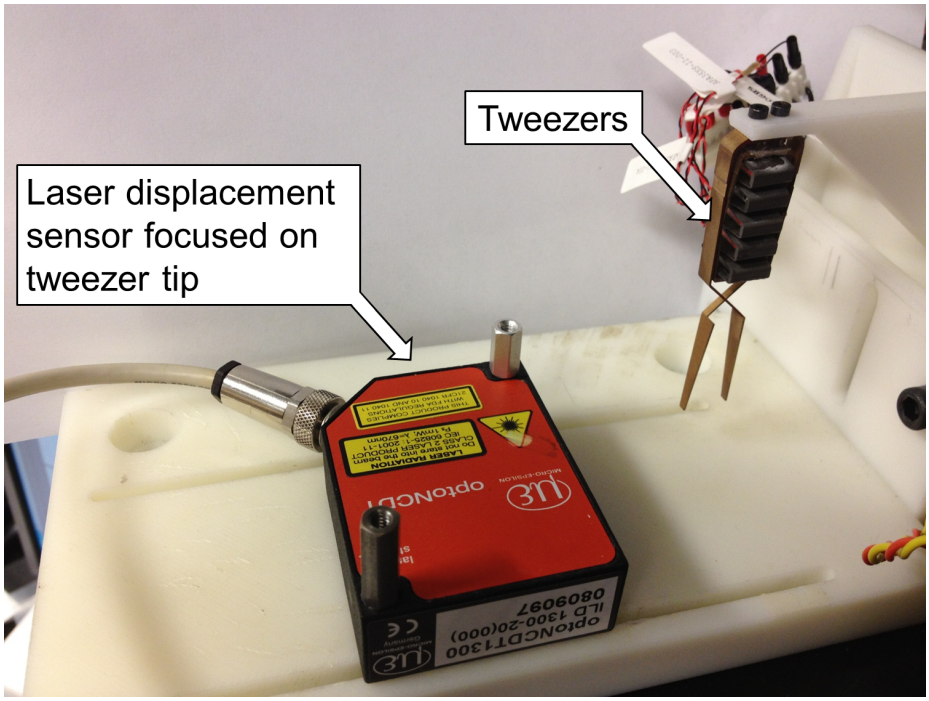

Figure 19: Experimental setup for displacement sensing

to output the control signal to the amplifier. Data was recorded at 1000 Hz, and the resolution was 162 μV for all measurements.

5.2 Experiments and Results

Force and displacement self-sensing were tested under a variety of loading conditions from fully blocked tweezer tips to fully free, as well as with various sizes of rigid objects used as a disturbances. First, the hysteresis operator H(q) was calibrated using data from the free case. Figure 21 shows the calibrated hysteresis operator $H(q)$. Fifteen elementary play, superposition, and creep operators were used. $H(q)$ shows a good match to the experimental data, with a maximum error of 3.34 V and an average error of 0.81 V, or 2.4% and 0.58% respectively of the output range.

Table 3 summarizes the performance of the self sensing technique. Figure 25 through 30 shows the self-sensed displacement versus the reference measurement for a variety of loading conditions. Note these figures show the estimation of $\Delta x_{pzt}/2$ since the laser sensor measures only one side of the tweezers. The displacement of the

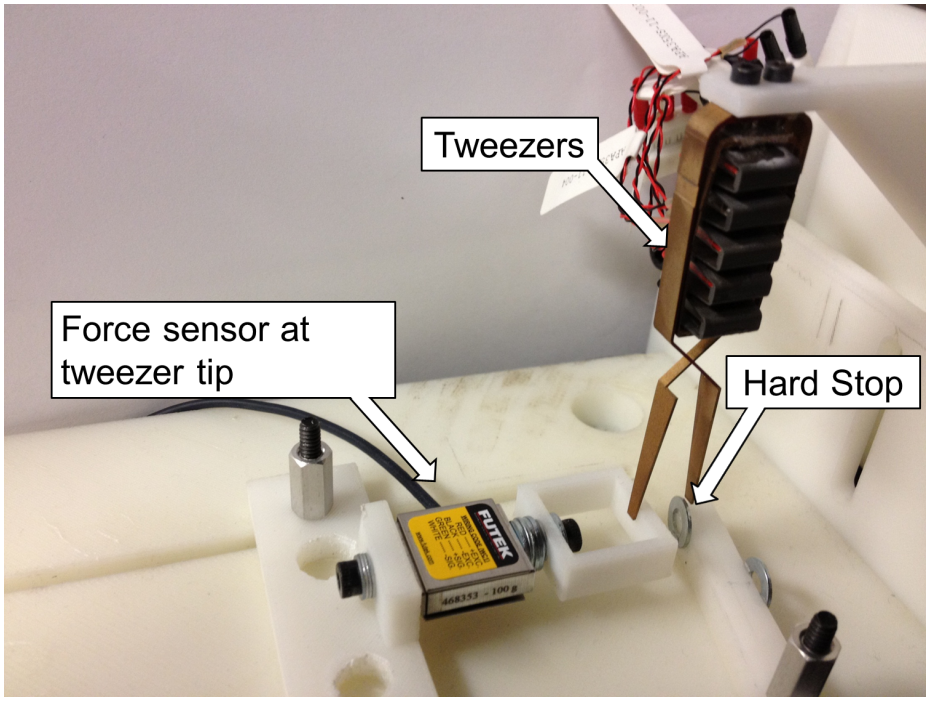

Figure 20: Experimental setup for force sensing

other side is assumed to be identical. Two simple techniques were implemented to slightly increase the accuracy. The force and displacement measurements were limited to their respective maximum and minimum values. Additionally, for the displacement measurement slight drift was removed with a sliding DC offset. The offset reset as the current displacement measurement whenever the input voltage was zero. Figure 24 shows the effect of these techniques. Two input signals were used, one purely sinusoidal shown in Fig. 22 and one a mixture of trapezoidal and sinusoidal inputs, shown in Fig. 23. The input signal in Fig. 22 was also used for the calibration of $H(q)$. The average accuracy of the self-sensed measurement is 12% of the dynamic range. Figures 25 through 30 shows the self sensed force and the reference measurement. The average accuracy of the self-sensed measurement is also 12% of the dynamic range.

Fig. 37 shows the force and displacement estimation from one trial with a common time axis. Notice that it agrees with what would be expected. Ideally, the force should be zero until the tip touches the disturbance, after which is should increase

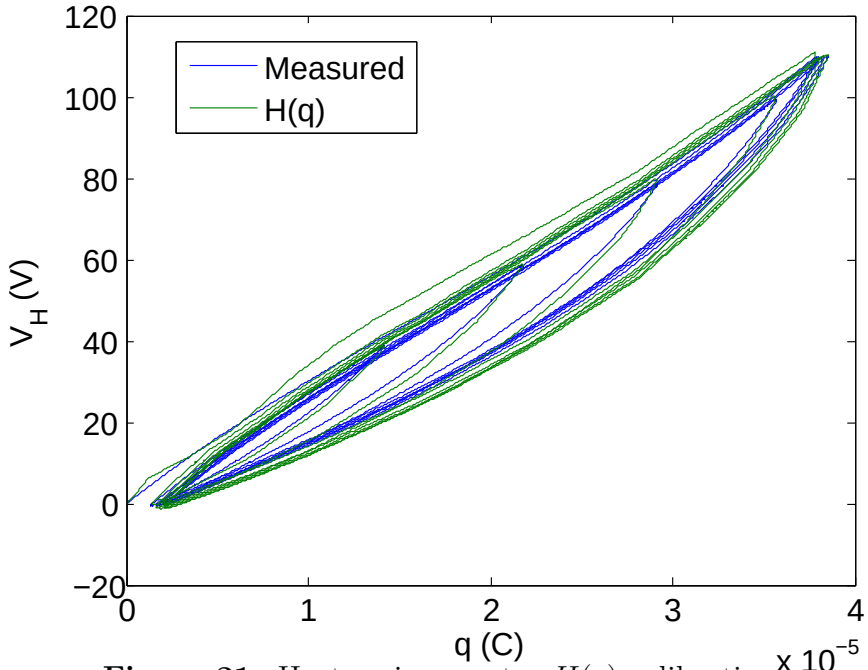

Figure 21: Hysteresis operator $H(q)$ calibration

Table 3: Performance of Self-Sensing Technique

Performance of Self-Sensing Technique		
Measurement	Mean Error	Mean Error Reported by Kurita et. al. [24]
Displacement	0.4 mm (12%)	11%
Force	0.012 N (12%)	11%

with increasing supply voltage. As the tip returns to its starting position the force decreases to zero until the tip is no longer in contact with the disturbance.

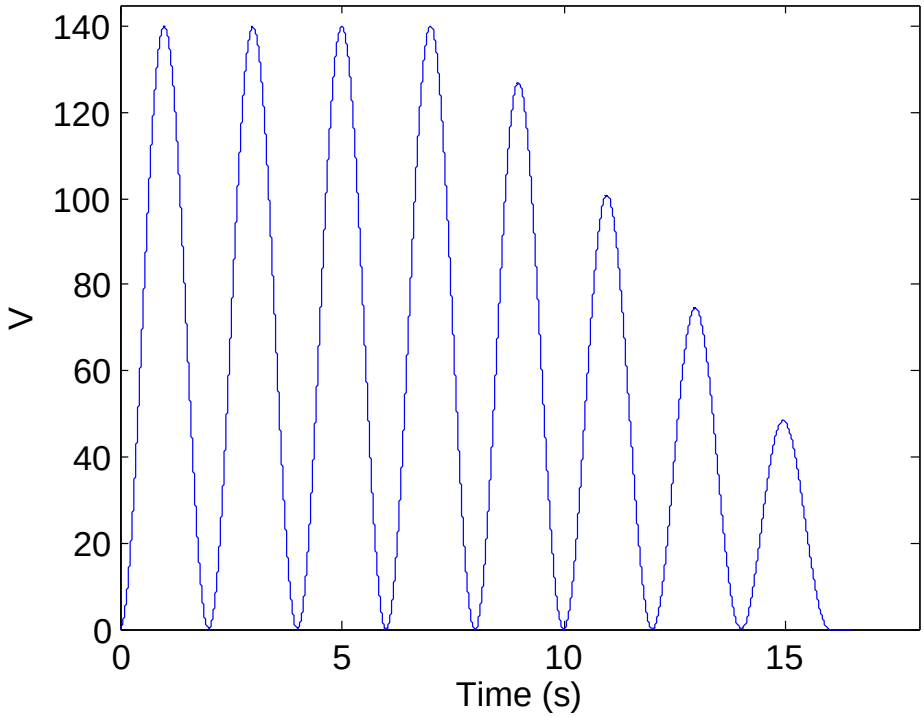

Figure 22: Sinusoidal Driving Voltage

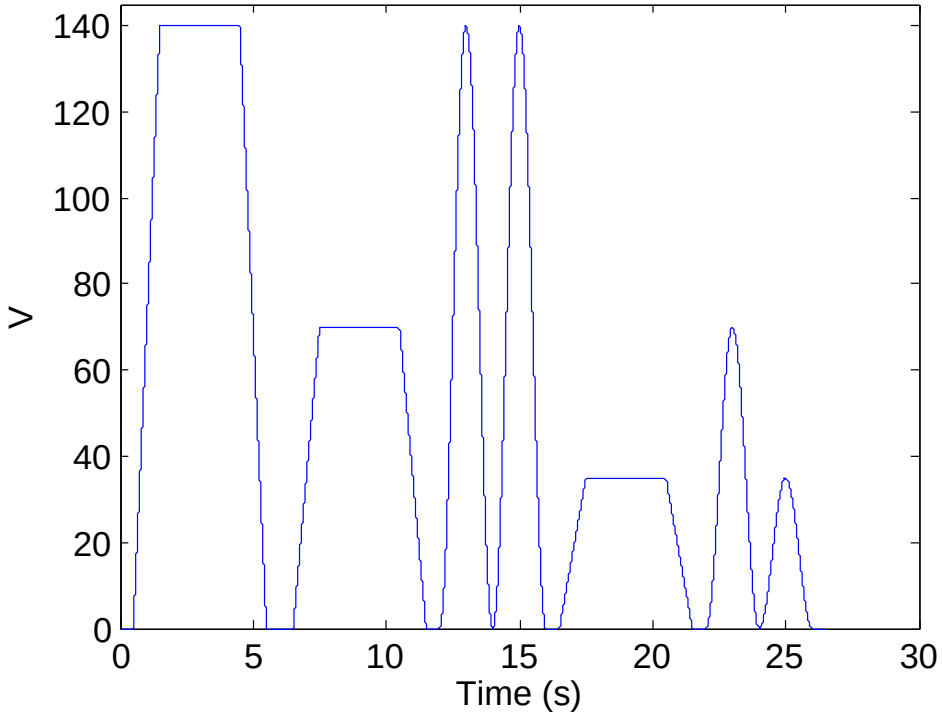

Figure 23: Mixed Trapezoidal and Sinusoidal Driving Voltage

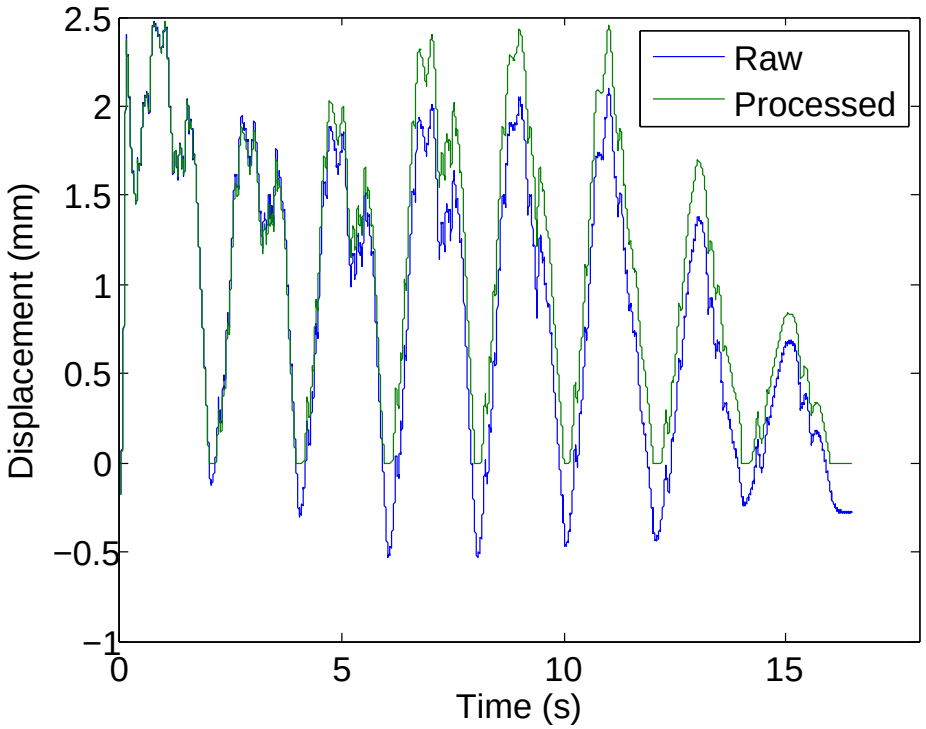

Figure 24: Effect of limiting and sliding DC offset

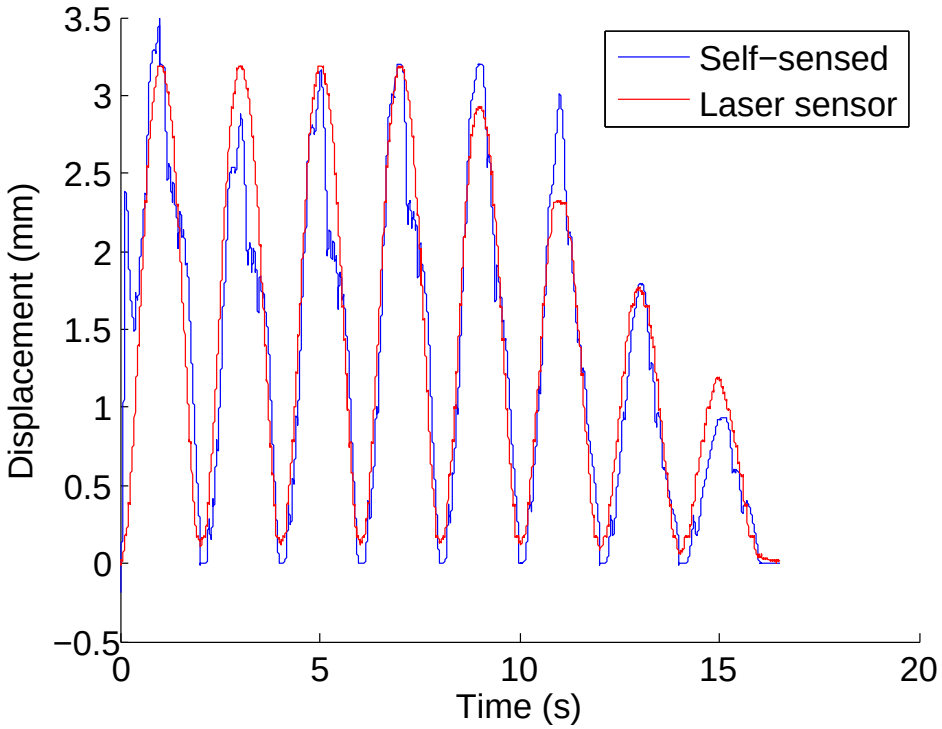

Figure 25: Displacement Data Trial 1: Free Tip

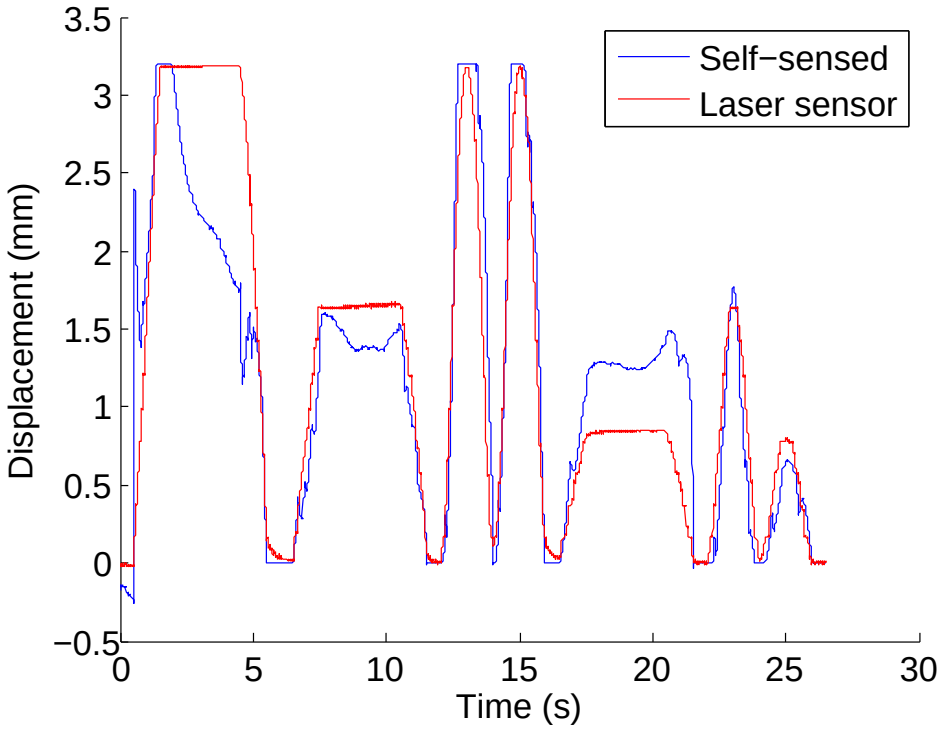

Figure 26: Displacement Data Trial 2: Free Tip

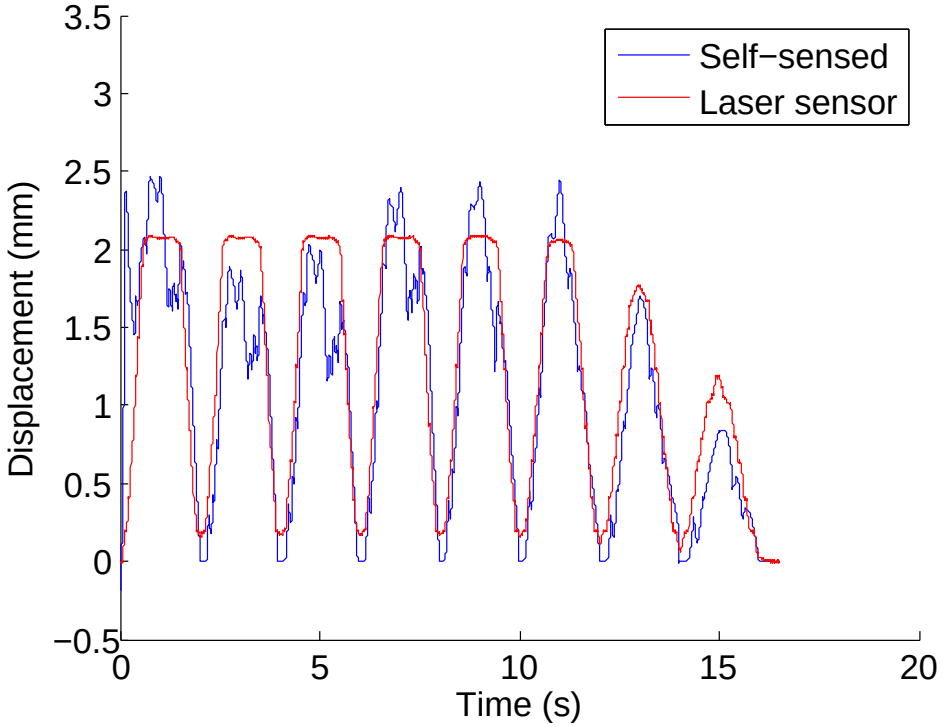

Figure 27: Displacement Data Trial 3: Small Disturbance

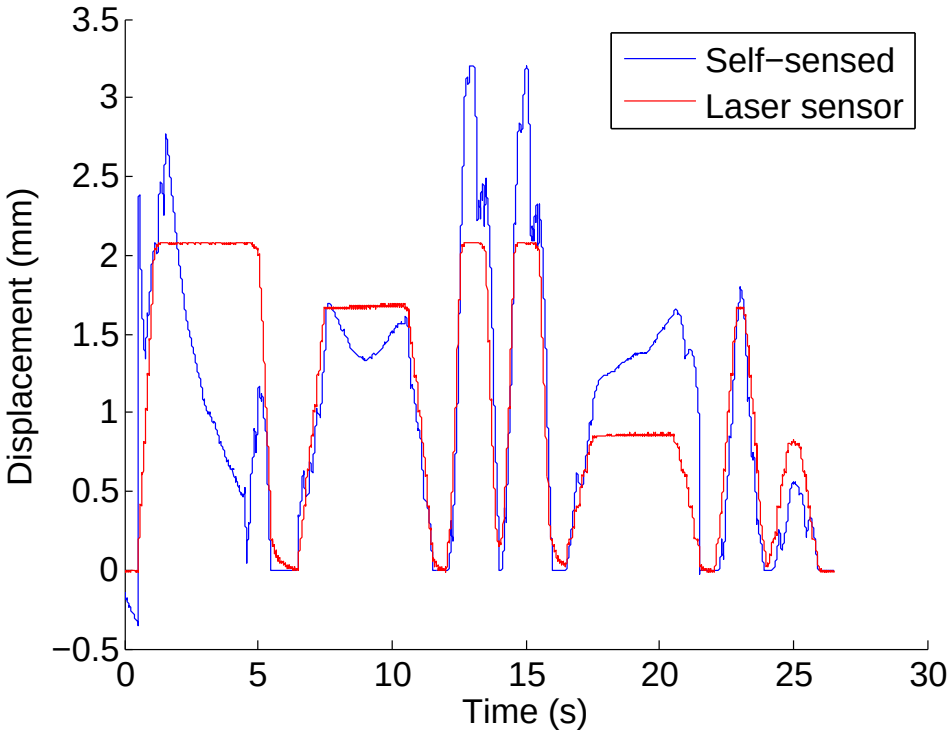

Figure 28: Displacement Data Trial 4: Small Disturbance

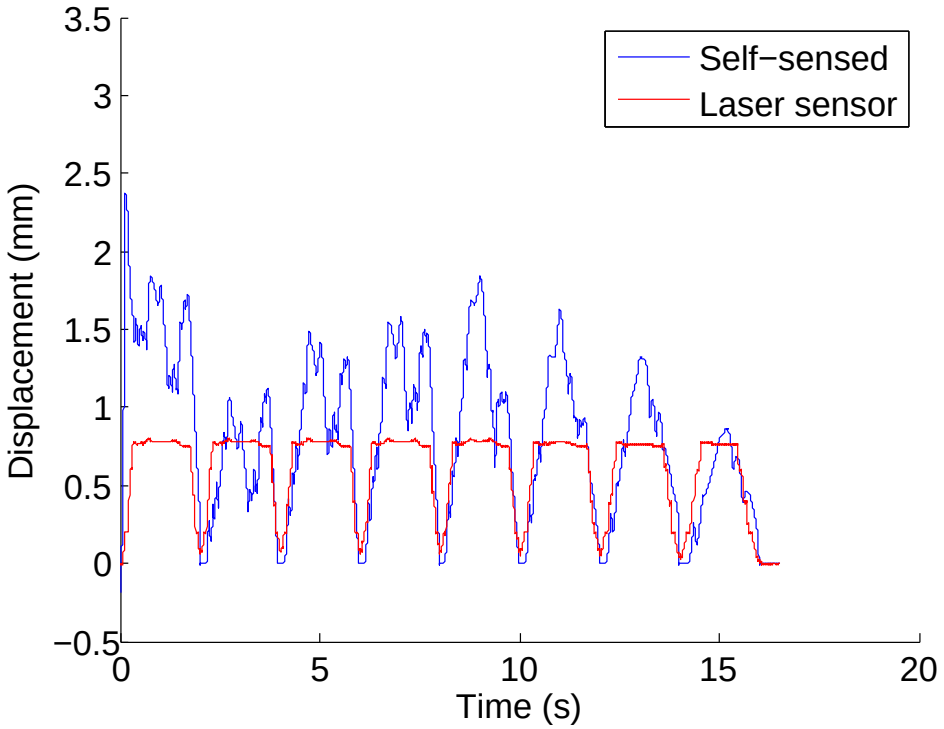

Figure 29: Displacement Data Trial 5: Large Disturbance

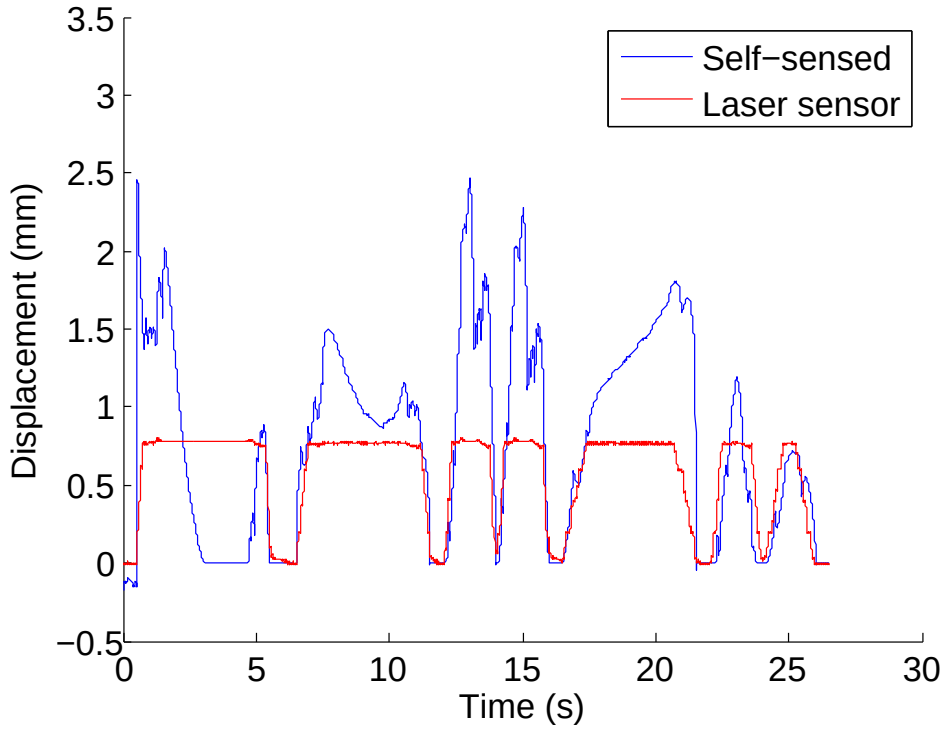

Figure 30: Displacement Data Trial 6: Large Disturbance

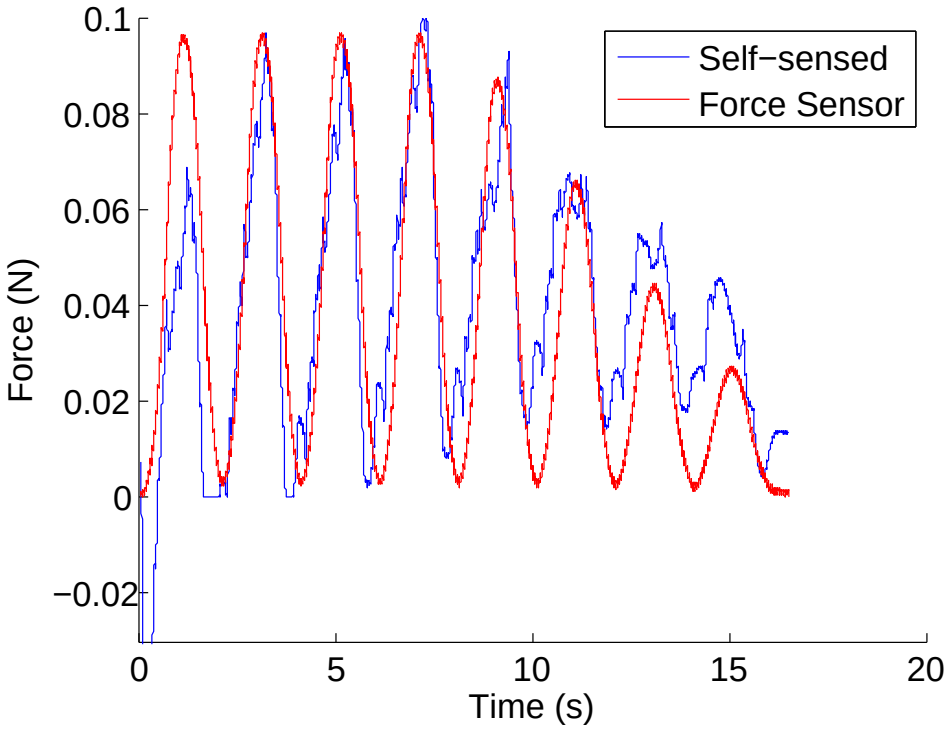

Figure 31: Force Data Trial 1: Fully Blocked Tip

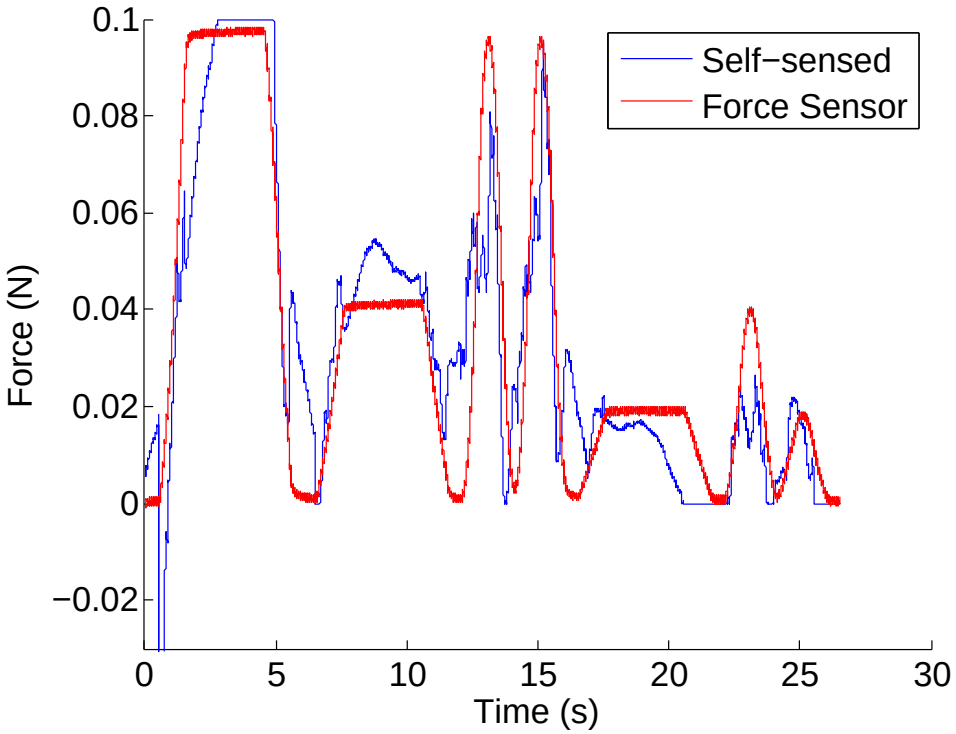

Figure 32: Force Data Trial 2: Fully Blocked Tip

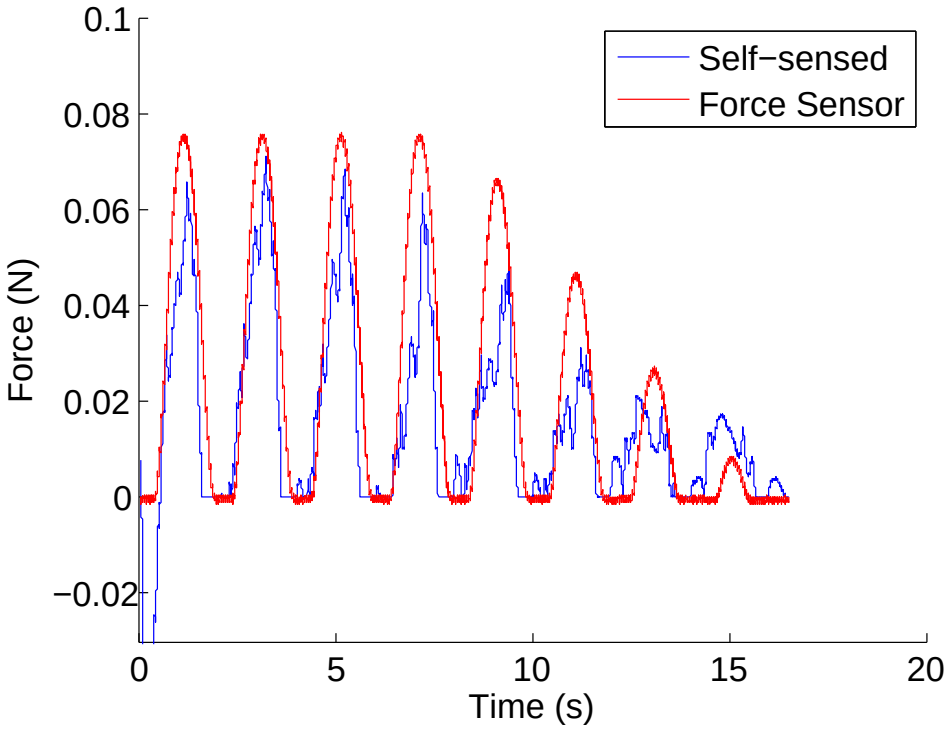

Figure 33: Force Data Trial 3: Large Disturbance

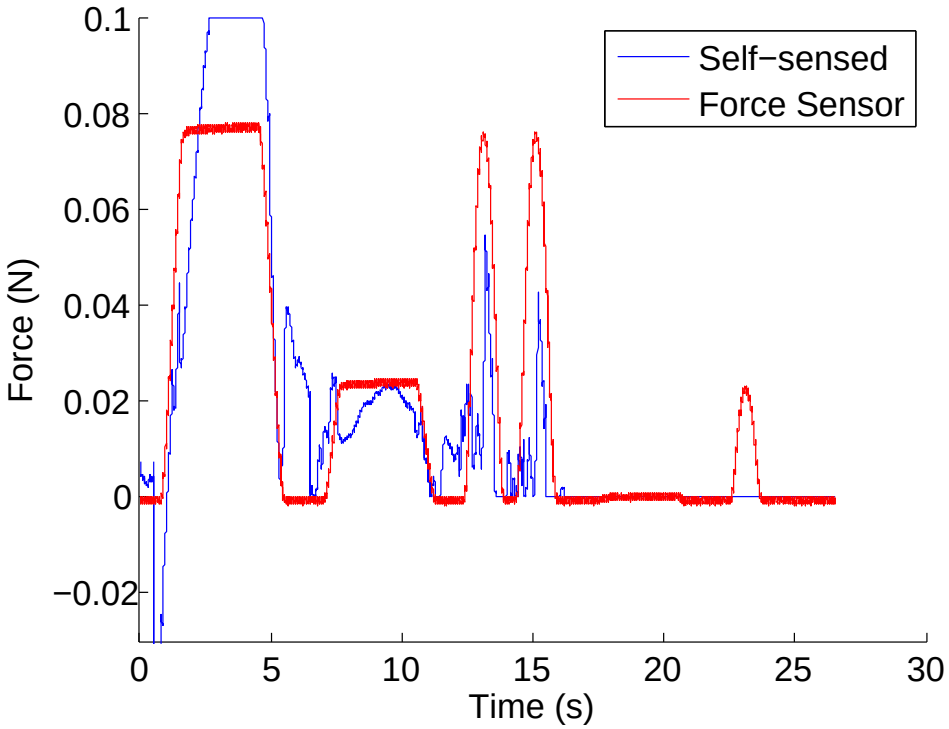

Figure 34: Force Data Trial 4: Large Disturbance

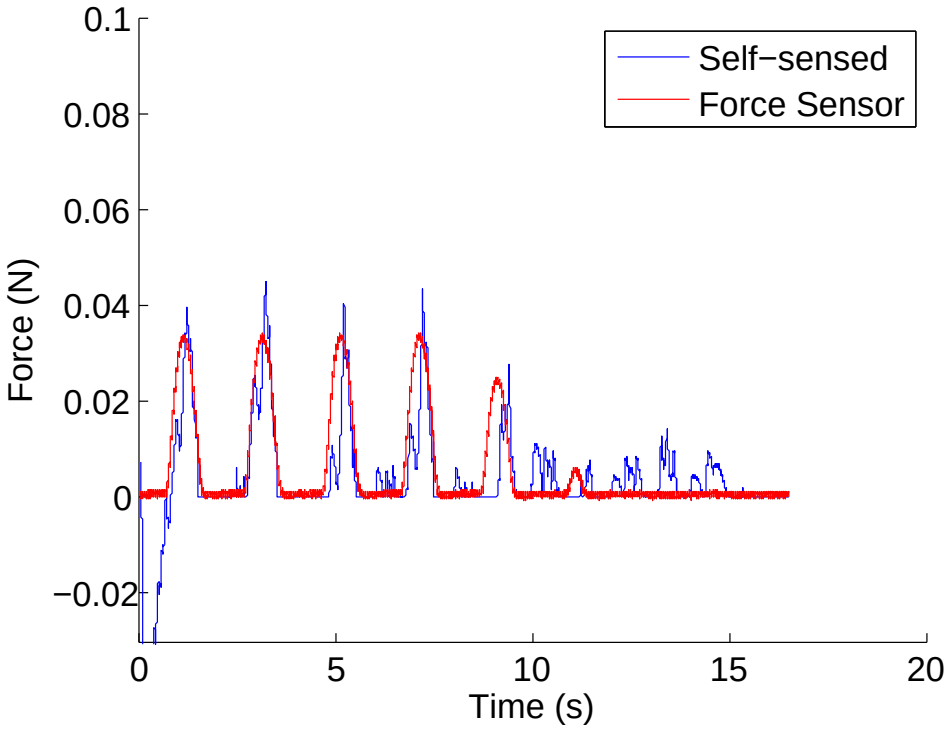

Figure 35: Force Data Trial 5: Small Disturbance

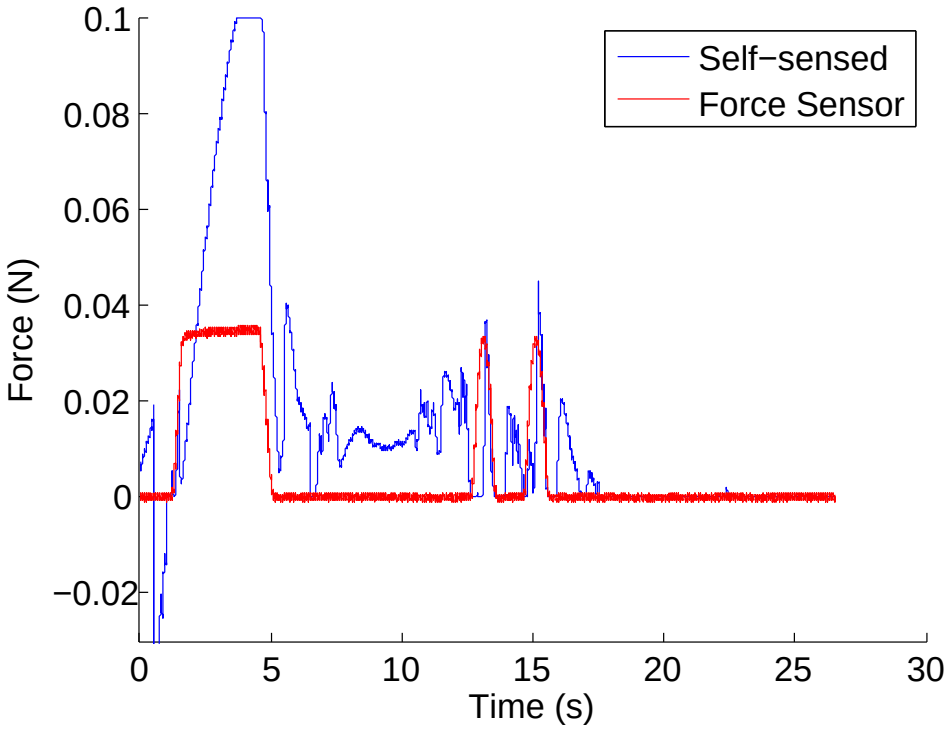

Figure 36: Force Data Trial 6: Small Disturbance

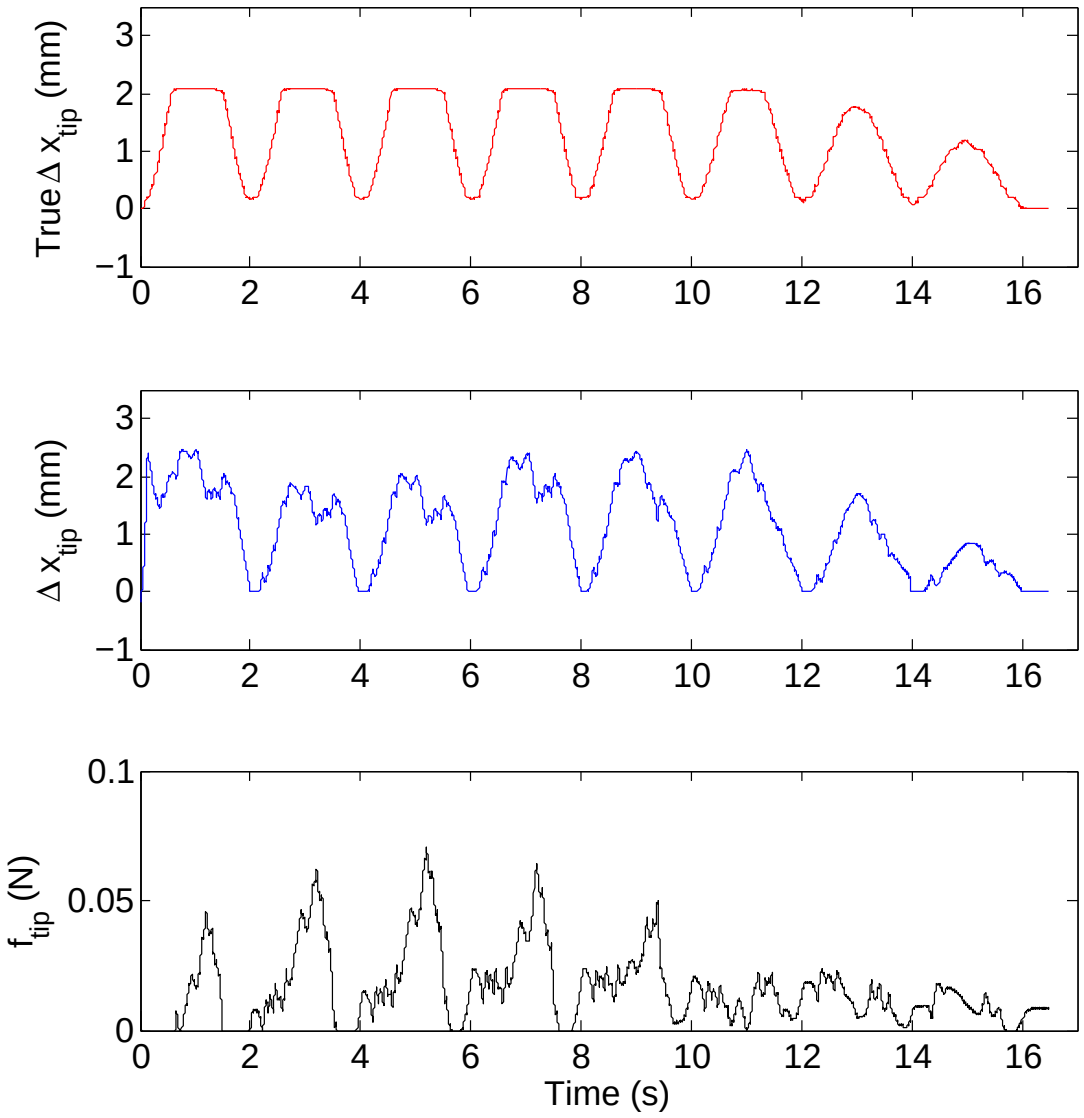

Figure 37: Force and Displacement Self-Sensed Signals

5.3 Discussion

Though error is present, the accuracy of the self-sensing method is comparable to that reported Kurita, et. al in an earlier study of the same device [24]. However, the sensing method developed in that work relied on prior knowledge of the loading condition as either fixed or free. The method presented here maintains a similar level of accuracy while greatly extending applicability by allowing for unknown tip conditions. However, the accuracy is lower than that reported by Badel et. al in [2], where a similar method was used but for a solitary PZT actuator. There are several

possible causes of error. First, the tweezers mechanism is very compliant. This means that a large change in displacement at the tip corresponds to a small change at the PZT actuator. Consider the simple mechanical system in Fig. 38, which represents a PZT actuator in series with a stiffness and serves to illustrate the effect in question. If the endpoint is free, the displacement of the midpoint is

$$\Delta x_{pzt} = \frac{f_{pzt}}{k_{pzt}} \tag{58}$$

If the endpoint is blocked the displacement becomes

$$\Delta x_{pzt} = \frac{f_{pzt}}{k_{pzt} + k_1} \tag{59}$$

If k_1 is small relative to k_{pzt} the displacements in the blocked and free cases will be very close to each other. The tweezer mechanism is more complicated than the system in Fig. 38, but the basic effect is the same, namely the displacement of the displacement of the PZT actuator will not vary much between the blocked and free cases. Charge is directly related to the displacement on the actuator and the applied voltage, based on (24). This means that for the same driving voltage a small change in the displacement, and subsequently charge, will cover the entire range of loading conditions at the tip. In effect, the signal to noise ratio is drastically worsened, meaning that not only the charge and voltage measurements but also the hysteresis model must be extremely accurate. In fact, despite the less than 1% average error of the hysteresis model, this mismatch is likely the main cause of error.

The force predicted by the self-sensing technique in the free case shows the effect of mismatch in the hysteresis model since this is the calibration case for the hysteresis operator. Therefore the effect of the mismatch on force prediction can be shown by subtracting this case from any other, given the same input voltage. Figure 39 shows a self-sensed force measurement, and the same measurement when the error due to model mismatch has been subtracted. This significantly improves the measurement, indicating that despite its relatively low error the hysteresis operator is the main

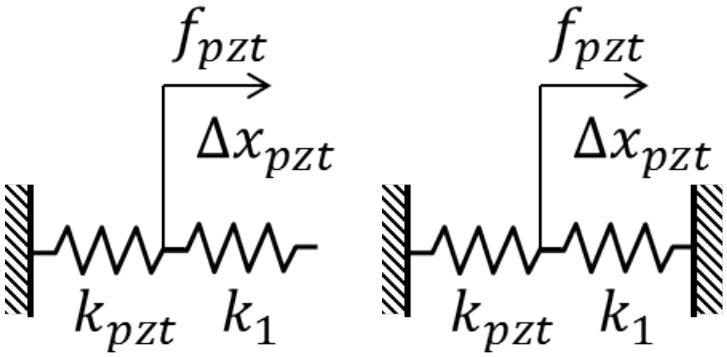

(a) Free (b) Blocked

Figure 38: A simple model of a PZT actuator and a stiffness in series

limiting factor of accuracy, rather than charge or voltage measurement. This indicates that for a robot with a set of preprogrammed motions, the model error could be calculated in advance and used to improve the sensing accuracy. For example, if the tweezer end effector was controlled by the push of a button to toggle between open or closed, the self sensing method could be used to obtain useful information such as the size of a grasped object. If the command is not known in advance, increasing the number elementary operators in the hysteresis model could provide a slight increase in accuracy, but this becomes computationally intensive and will reach a point of diminishing returns. Additionally, the creep effect is another source of error. Prior work on self sensing, even those assuming quasistatic operation, has been limited to a time scale of milliseconds, over which the effect of creep is negligible. For a robotic end effector the time scale of interest is seconds or minutes, at which point creep can no longer be ignored.

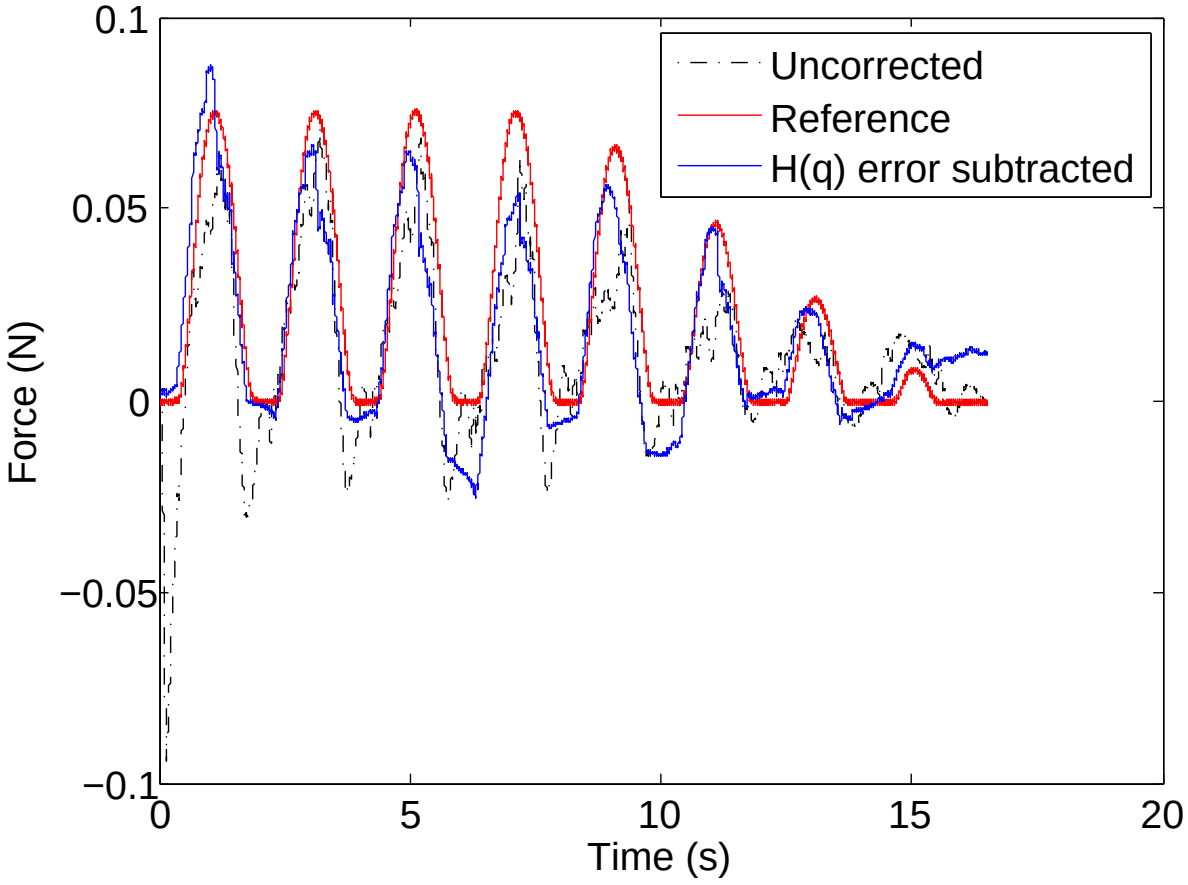

Figure 39: The effect of hysteresis model mismatch on accuracy

CHAPTER VI

CONCLUSION

A self-sensing technique has been developed that allows the force and displacement of a tweezer style end effector to be simultaneously estimated if voltage and charge are measured. This technique relies on a hysteretic piezoelectric model and two port network modeling of nested strain amplification mechanisms. The modified prandtl-ishlinksii approach was used to model hysteresis. Despite the method's accuracy, it was seen that hysteresis model mismatch was a major cause of error, due to the highly compliant tweezer structure. The force and displacement measurements were seen to have an average error of 12%, comparable to the much more limited method in [24]. Potential future work in this area could involve development of more advanced signal processing techniques to improve the accuracy of the estimation, as well extending the applicability of the sensing method to the dynamic case.

APPENDIX A

IDENTIFICATION PROCEDURE FOR THE MODIFIED PRANDTL-ISHLINKSII OPERATOR

$x(t)$ is a known input and $y(t)$ is measured output. The error between model and experiment can be expressed as

$$\begin{aligned} E[x,y](t) &= H[x](t) + K[x](t) - S^{-1}[y](t) \\ &= \boldsymbol{w}_H^T \cdot \boldsymbol{H}_{\boldsymbol{r}_H}[x, \boldsymbol{z}_{H0}](t) + \boldsymbol{w}_K^T \cdot \boldsymbol{K}_{\boldsymbol{r}_K \boldsymbol{a}_K}[x, \boldsymbol{Z}_{K0}](t) \cdot \boldsymbol{i} - \boldsymbol{w}_S'^T \cdot \boldsymbol{S}_{\boldsymbol{r}'_S}[y](t) \end{aligned} \tag{60}$$

Note that S^{-1} has the same form as S but with different weights. The threshold values are determined by the range of measured input and output values according to equations 61 and 62.

$$r_{Hi} = r_{Ki} = \frac{i}{n+1}\|x(t)\|_\infty \quad \text{for } i = 0, 1, \cdots, n \tag{61}$$

$$r'_{Si} = \begin{cases} 0 & \text{for } i = 0 \\ \dfrac{i - \frac{l}{2}}{l}\|y(t)\|_\infty & \text{for } i = 1, 2, \cdots, l \end{cases} \tag{62}$$

Recall the creep eigenvalues are defined in equation 40. Let t_0 be the initial time and t_f be the final time of the measurement data. Appropriate weights can be identified by finding those that minimize the square of the error integrated from t_0 to t_f. This gives

$$\boldsymbol{w}^* = \arg\min(V(\boldsymbol{w})) \tag{63}$$

$$V(\boldsymbol{w}) = \frac{1}{2}\int_{t_0}^{t_f} E[x,y](t)dt \tag{64}$$

$$= \frac{1}{2}\boldsymbol{w}^T \cdot \int_{t_0}^{t_f} \boldsymbol{Q}\boldsymbol{Q}^T dt \cdot \boldsymbol{w} \tag{65}$$

with

$$\boldsymbol{w} = \begin{bmatrix} \boldsymbol{w}_H \\ \boldsymbol{w}'_S \\ \boldsymbol{w}_K \end{bmatrix} \in \mathbb{R}^{2n+l+3} \tag{66}$$

$$\boldsymbol{Q}(t) = \begin{bmatrix} \boldsymbol{H}_{\boldsymbol{r}_H}[x, \boldsymbol{z}_{H0}](t) \\ \boldsymbol{S}_{\boldsymbol{r}'_S}[y](t) \\ \boldsymbol{K}_{\boldsymbol{r}_K \boldsymbol{a}_K}[x, \boldsymbol{Z}_{K0}](t) \cdot \boldsymbol{i} \end{bmatrix} \in \mathbb{R}^{2n+l+3} \tag{67}$$

$\boldsymbol{w}^*$ is the optimal set of weights. The optimization is subject to the inequality constraints

$$\boldsymbol{U} \cdot \boldsymbol{w} - u \leq \boldsymbol{o} \tag{68}$$

with

$$\boldsymbol{U} = \begin{bmatrix} \boldsymbol{U}_H & \boldsymbol{0} & \boldsymbol{0} \\ \boldsymbol{0} & \boldsymbol{U}_S & \boldsymbol{0} \\ \boldsymbol{0} & \boldsymbol{0} & \boldsymbol{U}_K \end{bmatrix} \in \mathbb{R}^{2n+l+3 \times 2n+l+3} \tag{69}$$

$$\boldsymbol{u} = \begin{bmatrix} \boldsymbol{u}_H \\ \boldsymbol{u}_S \\ \boldsymbol{u}_K \end{bmatrix} \in \mathbb{R}^{2n+l+3} \tag{70}$$

$$\boldsymbol{U}_H = \boldsymbol{U}_K = \begin{bmatrix} -1 & 0 & \cdots & 0 \\ 0 & -1 & \cdots & 0 \\ \vdots & \vdots & \ddots & \vdots \\ 0 & 0 & \cdots & -1 \end{bmatrix} \in \mathbb{R}^{n+1 \times n+1} \tag{71}$$

$$\boldsymbol{U}_S = \begin{bmatrix} -1 & -1 & \cdots & -1 \\ 0 & -1 & \cdots & -1 \\ \vdots & \vdots & \ddots & \vdots \\ 0 & 0 & \cdots & -1 \end{bmatrix} \in \mathbb{R}^{l+1 \times l+1} \tag{72}$$

$$\boldsymbol{u}_H^T = [-\epsilon \; 0 \; \cdots \; 0] \in \mathbb{R}^{n+1} \tag{73}$$

$$\boldsymbol{u}_S^T = [-\epsilon \ -\epsilon \ \cdots \ -\epsilon] \in \mathbb{R}^{l+1} \tag{74}$$

$$\boldsymbol{u}_K^T = [0 \ 0 \ \cdots \ 0] \in \mathbb{R}^{n+1} \tag{75}$$

$\epsilon > 0$ defines a lower bound for the weights, and can be any small number. $\boldsymbol{o}$ and $\boldsymbol{0}$ are vectors and matrices of zeros of appropriate size. The optimization is also subject to the equality constraint

$$\boldsymbol{q}^T \cdot \boldsymbol{w} - g = \boldsymbol{o} \tag{76}$$

where

$$\boldsymbol{g} = \begin{bmatrix} \|x\|_\infty \boldsymbol{i} - \boldsymbol{r}_H \\ \boldsymbol{o} \\ m\|x\|_\infty \boldsymbol{i} - m\boldsymbol{r}_K \end{bmatrix} \in \mathbb{R}^{2n+l+3} \tag{77}$$

and

$$g = \|x\|_\infty \tag{78}$$

The optimization returns the weights of the hysteresis and creep operators, and the weights of the inverse superposition operator.

$$\boldsymbol{w}_S = \begin{cases} w_{S0} = \dfrac{1}{w'_{S0}} \\ w_{Si} = -\dfrac{w'_{Si}}{\left(w'_{S0} + \sum\limits_{j=1}^{i} w'_{sj}\right)\left(w'_{S0} + \sum\limits_{j=1}^{i-1} w'_{sj}\right)} \quad i = 1, 2, \cdots, l \end{cases} \tag{79}$$

Additionally, the thresholds are determined by

$$r_{Si} = \sum_{j=0}^{i} w'_{Sj}(r'_{Si} - r'_{Sj}) \quad i = 0, 1, \cdots, l \tag{80}$$

If the calibration data is taken starting from a fully relaxed starting point, all initial conditions can be set to zero. In this case, however, the pre-load on the PZT actuator prevents this from occurring. The initial conditions can be set experimentally be starting with zeros, and then incrementing $\boldsymbol{z}_{H0}$ until the initial slope matches the experimental data. All terms in $\boldsymbol{z}_{H0}$ were assumed to be the same for simplicity. The weights were optimized numerically using the MATLAB command quadprog.

REFERENCES

[1] "Cedrat technologies piezo products catalouge," 2011.

[2] Badel, A., Qiu, J., and Nakano, T., "Self-sensing force control of a piezoelectric actuator," *IEEE Transactions on Ultrasonics, Ferroelectrics and Frequency Control*, vol. 55, pp. 2571–2581, 2008.

[3] Banning, R., de Koning, W. L., Adriaens, H. J., and Koops, R. K., "State-space analysis and identification for a class of hysteretic systems," *Automatica*, vol. 37, pp. 1883–1892, 2001.

[4] Belly, C., Mathieu, H., Claeyssen, F., and Letty, R. L., "Mri-compliant micro-motors for medical and biomedical applications," tech. rep., Cedrat Technologies, 2010.

[5] Brokate, M. and Sprekels, J., *Hysteresis and Phase Transistions*. Springer, 1996.

[6] Chinzei, K., Hata, N., Jolesz, F., and Kikinis, R., "Mr compatible surgical assist robot: system integration and preliminary feasibility study.," in *Proceedings of Medical Image Computing and Computer-assisted Intervention*, 2000.

[7] Chinzei, K., Kikinis, R., and Jolesz, F., "Mr compatibility of mechatronic devices: Design criteria," in *Proceedings of Medical Image Computing and Computer-assisted Intervention*, 1999.

[8] Dosch, J. J., Inman, D. J., and Garcia, E., "A self-sensing piezoelectric actuator for collocated control," *Journal of Intelligent Material Systems and Structures*, vol. 3, pp. 166–185, 1992.

[9] Dumoulin, C., Souza, S., and Darrow, R., "Real-time position monitoring of invasive devices using magnetic resonance," *Magnetic Resonance in Medicine*, vol. 29, pp. 411–415, 1993.

[10] Garnett E. Simmers, J., Hodgkins, J. R., Mascarenas, D. D., Park, G., and Sohn, H., "Improved piezoelectric self-sensing actuation," *Journal of Intelligent Material Systems and Structures*, vol. 15, pp. 941–953, 2004.

[11] Georgiou, H. M. and Mrad, R. B., "Electromechanical modeling of piezoceramic actuators for dynamic loading applications," *ASME Jornal of Dynamic Systems, Measurement, and Control*, vol. 128, pp. 558–567, 2006.

[12] Gerhardus, D., "Robot-assisted surgery: The future is here," *Journal of Healthcare Management*, vol. 4, pp. 242–251, 2003.

[13] Goldfarb, M. and Celanovic, N., "A lumped parameter electromechanical model for describing the nonlinear behavior of piezoelectric actuators," *ASME Jornal of Dynamic Systems, Measurement, and Control*, vol. 119, pp. 478–485, 1997.

[14] Hynynen, K., Darkazanli, A., Unger, E., and Schenck, J., "Mri-guided noninvasive ultrasound surgery," *Medical Physics*, vol. 20, pp. 107–115, 1992.

[15] Ivan, I. A., Rakotondrabe, M., Lutz, P., and Challiet, N., "Current integration force and displacement self-sensing method for catilevered piezoelectric actuators," *Review of Scientific Instruments*, vol. 80, pp. 126103–1–126103–3, 2009.

[16] Ivan, I. A., Rakotondrabe, M., Lutz, P., and Challiet, N., "Quasistatic displacement self-sensing method for cantilevered actuators," *Review of Scientific Instruments*, vol. 80, 2009.

[17] Jolesz, F., Nabavi, A., and Kikinis, R., "Integration of interventional mri with computer-assisted surgery," *Journal of Magnetic Resonance Imaging*, vol. 13, pp. 69–77, 2001.

[18] Kaiser, W. A., Fischer, H., Vagner, J., and Selig, M., "Robotic system for biopsy and therapy of breast lesions in a high-field whole-body magnetic resonance tomography unit," *Investagative Radiology*, vol. 35, pp. 513–519, 2000.

[19] Kholkin, A., Jadidian, B., and Safari, A., *Encyclopedia of Smart Materials*, vol. 1. John Wiley and Sons, 2002.

[20] Kim, D., Kobayashi, E., Dohi, T., and Sakuma, I., "A new, compact mr-compatible surgical manipulator for minimally invasive liver surgery," in *Proceedings of Medical Image Computing and Computer-assisted Intervention*, 2010.

[21] Kuhnen, K., "Modeling, identification,and compensation of complex hysteretic nonlinearities a modified prandtl-ishlinskii approach," *European Journal of Control*, vol. 9, pp. 407–418, 2003.

[22] Kuhnen, K., "Modeling, identification, and compensation of complex hysteretic and log(t)-type creep nonlinearities," *Control and Intelligent Systems*, vol. 33, pp. 134–147, 2005.

[23] Kuiper, S. and Schitter, G., "Active damping of a piezoelectric tube scanner using self-sensing piezo actuation," *Mechatronics*, vol. 20, pp. 656–665, 2010.

[24] Kurita, Y., Sugihara, F., Ueda, J., and Ogasawara, T., "Piezoelectric tweezer-type end-effector with force and displacement sensing capability," *IEEE/ASME Transactions on Mechatronics*, vol. 16, 2011.

[25] McVeigh, E., Guttman, M., Lederman, R., Li, M., Kocaturk, O., Hunk, T., Kozlov, S., and Horvath, K., "Real-tim interactive mri-guided cardiac surgery," *Magnetic Resonance in Medicine*, vol. 56, pp. 958–964, 2006.

[26] National Instruments Corporation, 11500 North Mopac Expressway, Austin, TX 78759, USA, *DAQ M Series Manual*, July 2008.

[27] Ohta, N., Furutani, K., and Mieda, Y., "Displacement monitoring of stacked piezoelectric actuator by observing induced charge," in *Proceedings of the 1st International Conference on Positioning Technology*, 2004.

[28] Schenck, J., "The role of magnetic susceptibility in magnetic resonance imaging: Mri magnetic compatibility of the first and second kinds," *The International Journal of Medical Physics*, vol. 23, pp. 815–850, 1995.

[29] Seifert, V., Zimmerman, M., Trantakis, C., Vitzhum, H.-E., Kuhnel, K., Raabe, A., Bootz, F., Schnieder, J.-P., Schmidt, F., and Dietrich, J., "Open mri-guided neurosurgery," *Acta Neurochirurgica*, vol. 141, pp. 455–464, 1999.

[30] Stoianovici, D., Patriciu, A., Petrisor, D., Mazilu, D., and Kavoussi, L., "A new type of motor: Pneumatic step motor," *IEEE/ASME Transactions on Mechatronics*, vol. 12, pp. 98–106, 2007.

[31] Tada, M. and Kanade, T., "Development of an mr-compatible optical force sensor," in *Proceedings of the International Conference of the IEEE Engineering in Medicine and Biology Society*, 2004.

[32] Takahashi, N., Tada, M., Ueda, J., Matsumoto, Y., and Ogasawara, T., "An optical 6-axis force sensor for brain function analysis using fmri," in *Proceedings of the IEEE International Conference on Sensors*, 2003.

[33] Tskos, N., Khanicheh, A., Christoforou, E., and Mavroidis, C., "Magnetic resonance compativle robotic and mechatronics systems for image-guided interventions and rehabilitation: A review study," *Annual Review of Biomedical Engineering*, vol. 9, pp. 351–387, 2007.

[34] Turkseven, M. and Ueda, J., "Design of an mri compatible haptic interface," in *Proceedings of the IEEE/RSJ Conference on Intelligent Robots and Systems*, 2011.

[35] Ueda, J., Secord, T. W., and Asada, H. H., "Large effective-strain piezoelectric actuators using nested cellular architechture with exponential strain amplification mechanisms," *IEEE/ASME Transactions on Mechatronics*, vol. 15, pp. 770–782, 2010.

[36] van Randeraat, J. and Setterington, R., eds., *Piezoelectric Ceramics*. Mullard Limited, 1974.

[37] Wang, Y., Cole, G., Su, H., Pilitsis, J., and Fischer, G., "Mri compatbility evaluation of a piezoelectric acutator system for a neural interventional robot," in *Proceedings of the 31st Annual International Conference of the IEEE EMBS*, 2009.